

# Weak lensing by line-of-sight halos as the origin of flux-ratio anomalies in quadruply lensed QSOs

Kaiki Taro Inoue<sup>1,2\*</sup> † and Ryuichi Takahashi<sup>3</sup>

<sup>1</sup>*Department of Science and Engineering, Kinki University, Higashi-Osaka, 577-8502, Japan*

<sup>2</sup>*Department of Physics, University of Oxford, Denys Wilkinson Building, Keble Road, OX1 3RH, UK*

<sup>3</sup>*Faculty of Science and Technology, Hirosaki University, 3 Bunkyo-cho, Hirosaki, Aomori 036-8561, Japan*

8 November 2018

## ABSTRACT

We explore the weak lensing effect by line-of-sight halos and sub-halos with a mass of  $M \lesssim 10^7 M_\odot$  in Quasi-Stellar Object (QSO)-galaxy strong lens systems with quadruple images in a concordant  $\Lambda$  cold dark matter universe. Using a polynomially fitted non-linear power spectrum  $P(k)$  obtained from  $N$ -body simulations that can resolve halos with a mass of  $M \sim 10^5 M_\odot$ , or structures with a comoving wavenumber of  $k \sim 3 \times 10^2 h\text{Mpc}^{-1}$ , we find that the ratio of magnification perturbation due to intervening halos to that of a primary lens is typically  $\sim 10$  per cent and the predicted values agree well with the estimated values for 6 observed QSO-galaxy lens systems with quadruple images in the mid-infrared band without considering the effects of substructures inside a primary lens. We also find that the estimated amplitudes of convergence perturbation for the 6 lenses increase with the source redshift as predicted by theoretical models. Using an extrapolated matter power spectrum, we demonstrate that small halos or sub-halos in the line-of-sight with a mass of  $M = 10^3 - 10^7 M_\odot$ , or structures with a comoving wavenumber of  $k = 3 \times 10^2 - 10^4 h\text{Mpc}^{-1}$  can significantly affect the magnification ratios of the lensed images. Flux ratio anomalies in QSO-galaxy strong lens systems offer us a unique probe into clustering property of minihalos with a mass of  $M < 10^6 M_\odot$ .

**Key words:** cosmology: theory - gravitational lensing - dark matter - galaxies: formation

## 1 INTRODUCTION

Gravitational lensing is one of the most powerful tools for directly probing the structure and the distribution of dark matter. The remarkable agreement between the predicted and the observed weak lensing effects by large-scale structures or clusters provides independent and consistent estimates of clustering property of dark matter on cosmic scales  $\gtrsim 10 h^{-1}\text{Mpc}$ . However, we do not fully understand the clustering property on scales below  $\sim 1 h^{-1}\text{Mpc}$ , which correspond to individual galaxy halos. Although the cold dark matter (CDM) model predicts a large population of minihalos ( $\lesssim 10^7 M_\odot$ ), the observed number of dwarf galaxies in our galaxy seems too low in comparison with the predicted value. The discrepancy may be alleviated by some baryonic process, such as suppression of star formation by background UV radiation in the reionization epoch (e.g., Bullock et al. (2000), Busha et al. (2010)), or tidal disruption

due to a galactic disk (D’Onghia et al. 2010). Alternatively, the suppression of the number count might be associated with super-weakly interacting massive particles (super-WIMPs) or warm dark matter which has a larger free-streaming length than CDM (Hisano et al. 2006). In order to probe the clustering property of dark matter at mass scales of  $\lesssim 1 h^{-1}\text{Mpc}$ , strong QSO-galaxy lensing systems with quadruple images have been used in literature (Metcalf & Madau 2001; Chiba 2002). In fact, the flux ratios in some quadruply lensed QSOs disagree with the prediction of best-fit lens models with a potential whose fluctuation scale is larger than the separation between the lensed images. Such a discrepancy called the “anomalous flux ratio” has been considered as an imprint of substructure inside a lensing galaxy (Mao & Schneider 1998; Metcalf & Madau 2001; Metcalf et al. 2004; Chiba et al. 2005; Sugai et al. 2007; McKean et al. 2007; More et al. 2009; Minezaki et al. 2009; MacLeod et al. 2009).

However, recent studies based on high resolution simulations suggested that the predicted substructure population is too low to explain the observed anomalous flux ra-

\* E-mail: kinoue@phys.kindai.ac.jp

† E-mail: Kaiki.Inoue@astro.ox.ac.uk

tios (Maccio & Miranda 2006; Amara et al. 2006; Xu et al. 2009, 2010; Chen 2009; Chen et al. 2011). More detailed modeling of gravitational potential of the lens on scales comparable to or larger than the distance between the lensed images might also improve the fit (Wong et al. 2011). However, the origin of the anomalous flux ratios in some quadruple image systems such as B1422+231 and MG0414+0534 has been veiled in mystery (Chiba et al. 2005; Minezaki et al. 2009).

In addition to substructures in lensing galaxy, any intergalactic halos along the entire line-of-sight from the source to the observer can perturb the lensing potential. Therefore, they may change the flux ratios of the lensed images. Chen et al. (2003) have found that the contribution from intergalactic halos modeled as singular isothermal spheres would be  $\lesssim 10\%$  of that from substructures within the lensing halo. Metcalf (2005a) performed ray-tracing simulations for intergalactic halos with a mass of  $10^6 M_\odot \leq M \leq 10^9 M_\odot$ . Assuming that the halos have Navarro, Frenk & White (NFW) (Navarro et al. 1997) profiles and the number density is given by the Press-Schechter mass function (Press & Schechter 1974), he found that four radio lensed QSOs that shows a strong cusp-caustic violation are consistent with the predicted values without any substructures in the lensing galaxy. Assuming that halo profiles are modeled as singular isothermal spheres and the number density is given by the Sheth-Tormen mass function (Sheth & Tormen 2002), Miranda & Maccio (2007) obtained a similar conclusion for three radio and two optical/IR lensed QSOs. Using a  $N$ -body simulation that can resolve halos with a mass of  $> 10^8 h^{-1} M_\odot$ , and halos with a mass ( $10^6 M_\odot \leq M \leq 10^8 M_\odot$ ) whose number density obeys the Sheth-Tormen mass function, Xu et al. (2012) obtained a result that violation of the cusp-caustic relation caused by line-of-sight halos are comparable to (even larger than) those caused by intrinsic substructures though it depends sensitively on the halo profile.

In order to estimate the magnification perturbation due to intervening halos more precisely, it is important to take into account various effects that have been overlooked in literature. Firstly, if the shifts in relative positions of images and lens due to line-of-sight halos are too large, fitting a model with a smooth potential to the observed data becomes difficult since such a change is a consequence of a local effect. Moreover, even if the individual perturbing halo is not so massive, clustering halos could produce larger image shifts. Therefore, we need to incorporate the effects of clustering as well as the shifts of position of images and lens. Accuracy in observed positions of lensed images and lens would give an upper limit on the mass scale of perturbing halos. Secondly, in some lens systems, violation of the cusp-caustic relation might be caused by relatively massive faint satellite galaxies in the neighborhood of the lensing galaxy (McKean et al. 2007; Shin & Evans 2008; MacLeod et al. 2009). Therefore, application of the cusp-caustic relation to generic lensed QSO systems may not be appropriate. Instead, we need to use other statistics to fit the model. Thirdly, the effects of massive line-of-sight halos should be subtracted off since they can contribute to low-order components in magnification tensor such as a constant convergence and an external shear in the lens model. Otherwise, we would estimate

anomalies in the flux ratios systematically large because of double counting.

In this paper, we explore the weak lensing effect due to line-of-sight halos in QSO-galaxy lensing systems taking these three effects into account and study how it will affect the flux ratios of lensed QSOs with quadruple images. To take into account of halo clustering, we use  $N$ -body simulations to calculate the non-linear power spectrum of matter fluctuations down to mass scales of  $\sim 10^5 h^{-1} M_\odot$ . For simplicity, however, we do not put baryons in our  $N$ -body simulations. Then we estimate the magnification perturbation using the obtained non-linear power spectrum and study whether observed lensed QSO systems with quadruple images are consistent with our model prediction. In section 2, we describe magnification perturbation due to line-of-sight halos. In section 3, we derive analytic formulae for the power spectrum of convergence due to line-of-sight halos constrained from perturbations in image shifts. In section 4, we describe our  $N$ -body simulations for obtaining the non-linear power spectrum. In section 5, image shifts and magnification perturbation are investigated using a semi-analytic method developed in section 3. In Section 6, we describe 6 samples of QSO-galaxy lensing systems with quadruple images observed in the mid infrared (MIR) band. In section 7, we present our results on the flux ratio anomalies using these lens systems. In section 8, we conclude and discuss some relevant issues. In what follows, we assume a cosmology with a matter density  $\Omega_m = 0.272$ , a baryon density  $\Omega_b = 0.046$ , a cosmological constant  $\Omega_\Lambda = 0.728$ , the Hubble constant  $H_0 = 70$ , km/s/Mpc, the spectrum index  $n_s = 0.97$ , and the root-mean-square (rms) amplitude of matter fluctuations at  $8h^{-1}$  Mpc,  $\sigma_8 = 0.81$ , which are obtained from the observed CMB (WMAP 7yr result, (Jarosik et al. 2011)), the baryon acoustic oscillations (Percival et al. 2010), and  $H_0$  (Riess et al. 2009).

## 2 PERTURBATION OF MAGNIFICATION

Suppose a QSO at redshift  $z_S$  is lensed by a primary lensing galaxy at  $z_L$  to produce multiple images  $X_i$  and less massive intergalactic halos (secondary lenses) perturb the QSO-galaxy lens system. In what follows, we assume that the size of a light source is sufficiently small in comparison with the Einstein radius of the primary lens and those of perturbers in the line-of-sight. Choosing coordinates centered at a primary lens, given the angular position of a point on the source  $\theta_y$ , the angular position of the source  $\theta_x$  lensed by the primary lens and the intergalactic halos is approximately given by the lens equation defined at multiple lens planes  $n = 1, 2, \dots, N$  (see Fig. 1),

$$D_S \theta_y = D_S \theta_x - \sum_{n=1}^N D_{n,S} \hat{\alpha}_n(\mathbf{x}_n), \quad (1)$$

where  $D_S$  and  $D_{n,S}$  are the angular diameter distances between an observer and the source, the  $n$ th lens plane and the source, respectively, and  $\hat{\alpha}_n$  and  $\mathbf{x}_n$  are the deflection angle caused by a perturber and the two-dimensional position vector in the proper coordinates at the  $n$ th lens plane,

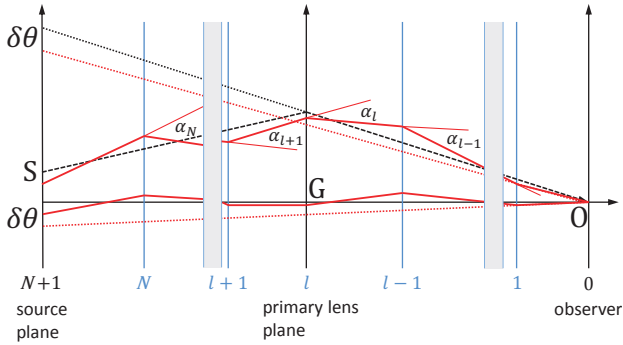


**Figure 1.** Schematic diagram of ray tracing through multiple lens planes. Unperturbed light ray (dashed lines) starts from a source S and is deflected by the primary lens galaxy G at the primary lens (the  $l$ th) plane and ends at O, a position of an observer. The light ray is perturbed by intergalactic halos in the line-of-sight (full curves).  $\hat{\alpha}_n$  is the deflection angle at the  $n$ th lens plane for  $n = 1, 2, \dots, N$ .  $\epsilon$  is the shift of image position or that of the center of primary lens.

respectively.  $\mathbf{x}_n$ 's satisfy

$$\mathbf{x}_n = \begin{cases} D_{01}\boldsymbol{\theta}_x, & n = 1 \\ D_{0i}\boldsymbol{\theta}_x - \sum_{m=1}^{n-1} D_{m,n}\hat{\boldsymbol{\alpha}}_m(\mathbf{x}_m), & 1 < n \leq N, \end{cases} \quad (2)$$

where  $D_{01}$  and  $D_{n,m}$  are the angular diameter distances between an observer and the first lens plane, and between the  $n$ th lens and the  $m$ th lens planes, respectively. We assume that the primary lens is placed at the  $l$ th plane. In general, it is difficult to solve equations (1) and (2) since the position  $\mathbf{x}_n$  depends on any other positions  $\mathbf{x}_m$ ,  $m \neq n$ . However, if the spatial derivatives of deflection angles are sufficiently small that

$$\left| \frac{\Delta \hat{\boldsymbol{\alpha}}_n}{|\hat{\boldsymbol{\alpha}}_n|} \right| = \left| \frac{\partial \hat{\boldsymbol{\alpha}}_n}{\partial \mathbf{x}_n} \cdot \hat{\boldsymbol{\alpha}}_n \right| \frac{D_{n,n+1}}{|\hat{\boldsymbol{\alpha}}_n|} \ll 1, \quad (3)$$

is satisfied, then the light ray approximately follows an unperturbed geodesic

$$\mathbf{x}_n \approx \begin{cases} D_{0n}\boldsymbol{\theta}_x, & n \leq l \\ D_{0n}\boldsymbol{\theta}_x - D_{l,n}\hat{\boldsymbol{\alpha}}_l(D_L\boldsymbol{\theta}_x), & n > l, \end{cases} \quad (4)$$

and each deflection angle  $\hat{\boldsymbol{\alpha}}_n$  depends only on the position vector  $\mathbf{x}_n$  that is independent of the other position vectors. This greatly simplifies the lens equations (1) and (2) since each  $\hat{\boldsymbol{\alpha}}_n$  becomes independent each other. In what follows, we assume that equation (3) holds in our lensing systems. Then the inverse of the magnification tensor is approximately given by

$$M^{-1} = \frac{\partial \boldsymbol{\theta}_y}{\partial \boldsymbol{\theta}_x} \approx \mathbf{1} - \frac{\partial \boldsymbol{\alpha}_l(\mathbf{x}_l)}{\partial \boldsymbol{\theta}_x} - \sum_{n \neq l} \frac{\partial \boldsymbol{\alpha}_n(\mathbf{x}_n)}{\partial \boldsymbol{\theta}_x}, \quad (5)$$

where  $\boldsymbol{\alpha}_n = D_{n,N+1}D_S^{-1}\hat{\boldsymbol{\alpha}}_n$ .

In terms of convergence  $\kappa_i$  and shear  $\gamma_{i1}$  and  $\gamma_{i2}$  due to the primary lens at the position of a point-like lensed image  $X_i$  where  $i$  denotes the index number of lensed images, the contribution from the primary lens can be written as

$$\Gamma_i = \frac{\partial \boldsymbol{\alpha}_l(\mathbf{x}_l)}{\partial \boldsymbol{\theta}_x} = \begin{bmatrix} \kappa_i + \gamma_{i1} & \gamma_{i2} \\ \gamma_{i2} & \kappa_i - \gamma_{i1} \end{bmatrix}. \quad (6)$$

In a similar manner, in terms of perturbations of convergence  $\delta\kappa$  and shear  $\delta\gamma_1, \delta\gamma_2$ , the contribution from clustering dark matter in the line-of-sight can be written as

$$\delta\Gamma = \sum_{i \neq l} \frac{\partial \boldsymbol{\alpha}_i(\mathbf{x}_i)}{\partial \boldsymbol{\theta}_x} = \begin{bmatrix} \delta\kappa + \delta\gamma_1 & \delta\gamma_2 \\ \delta\gamma_2 & \delta\kappa - \delta\gamma_1 \end{bmatrix}. \quad (7)$$

The approximated lens equation at each image position is then

$$\boldsymbol{\theta}_y = (\mathbf{1} - \Gamma_i - \delta\Gamma)\boldsymbol{\theta}_x. \quad (8)$$

In the following, we assume that perturbations of flux of images due to shifts of positions are sufficiently smaller than those due to distortion of the images. Then the perturbed magnification matrix is given by

$$\begin{aligned} (\mu_i + \delta\mu_i)^{-1} &= (1 - \kappa_i - \gamma_{i1} - \delta\kappa - \delta\gamma_1) \\ &\times (1 - \kappa_i + \gamma_{i1} - \delta\kappa + \delta\gamma_1) - (\gamma_{i2} + \delta\gamma_2)^2, \end{aligned} \quad (9)$$

where  $\mu_i^{-1} = (1 - \kappa_i)^2 - \gamma_{i1}^2 - \gamma_{i2}^2$ . A magnification contrast for image  $X_i$  is defined by  $\delta_i^\mu \equiv \delta\mu_i/\mu_i$ .

Up to linear order in  $\mu_i\delta\kappa$ ,  $\mu_i\delta\gamma_1$ , and  $\mu_i\delta\gamma_2$ , the magnification contrast is approximated as

$$\delta_i^\mu \approx \frac{2(1 - \kappa_i)\delta\kappa + 2\gamma_{i1}\delta\gamma_1 + 2\gamma_{i2}\delta\gamma_2}{(1 - \kappa_i)^2 - (\gamma_{i1}^2 + \gamma_{i2}^2)}, \quad (10)$$

which can be written as

$$\delta_i^\mu \approx \frac{2(1 - \kappa_i)\delta\kappa + 2\gamma_{i1}\delta\gamma_1}{(1 - \kappa_i)^2 - \gamma_{i1}^2}, \quad (11)$$

if magnification matrix for the primary lens is diagonalized (i.e.,  $\gamma_{i2} = 0$ ).

We expect that line-of-sight structures that significantly perturb the fluxes of images are relatively massive halos, which add  $\delta\kappa > 0$  to the background convergence. Assuming matter fluctuations that are homogeneous and isotropic, the mean of the shear perturbation is vanishing but the root-mean-square value is expected to be (Bartelmann & Schneider 2001)

$$\sqrt{\langle (\delta\gamma_1)^2 \rangle} = \sqrt{\langle (\delta\gamma_2)^2 \rangle} = \sqrt{\langle (\delta\kappa)^2 \rangle} / \sqrt{2}. \quad (12)$$

Therefore, in what follows, we assume that the shear perturbations satisfy

$$-\delta\kappa/\sqrt{2} < \delta\gamma_j < \delta\kappa/\sqrt{2}, \quad j = 1, 2. \quad (13)$$

The sign of magnification contrast depends on the curvature of the arrival time surface where the arrival time is stationary. If the arrival time is locally minimum, i.e.,  $(1 - \kappa_i)^2 - \gamma_{i1}^2 > 0$  and  $1 - \kappa_i > 0$ , the density contrast satisfies

$$\delta_i^\mu(\text{minima}) > \frac{(2 - \sqrt{2})\gamma_{i1}\delta\kappa}{(1 - \kappa_i)^2 - \gamma_{i1}^2}, \quad (14)$$

since  $1 - \kappa_i > \gamma_{i1}$ . As one can always choose local coordinates in which  $\gamma_{i1} > 0$ , we have  $\delta_i^\mu > 0$ . If the arrival time is locally maximum, i.e.,  $(1 - \kappa_i)^2 - \gamma_{i1}^2 > 0$  and  $1 - \kappa_i < 0$ , we have

$$\delta_i^\mu(\text{maxima}) < -\frac{(2 - \sqrt{2})\gamma_{i1}\delta\kappa}{(1 - \kappa_i)^2 - \gamma_{i1}^2}, \quad (15)$$

since  $1 - \kappa_i < \gamma_{i1}$ , leading to  $\delta_i^\mu < 0$ . Thus *strongly lensed images generated at a locally minimum/maximum point are*

magnified/demagnified definitely by intervening massive halos. If a stationary point in the arrival time surface is a saddle one, i.e.,  $(1 - \kappa_i)^2 - \gamma_i^2 < 0$ , we have  $1 - \kappa_i < \gamma_i$  and  $1 - \kappa_i > -\gamma_i$  as we assume  $\gamma_i > 0$ . Then the magnification contrast satisfies

$$\frac{(2 - \sqrt{2})\gamma_i\delta\kappa}{(1 - \kappa_i)^2 - \gamma_i^2} < \delta_i^\mu(\text{saddle}) < -\frac{(2 - \sqrt{2})\gamma_i\delta\kappa}{(1 - \kappa_i)^2 - \gamma_i^2}. \quad (16)$$

Therefore, the sign of magnification contrast cannot be determined definitely without additional conditions whereas the mean value is positive  $\langle \delta_i^\mu \rangle > 0$  for  $1 - \kappa_i < 0$  and negative  $\langle \delta_i^\mu \rangle < 0$  for  $1 - \kappa_i > 0$ . If the background convergence satisfies a condition  $2|(1 - \kappa_i)| > \sqrt{2}\gamma_i$ , then the magnification contrast has a definite sign  $\delta_i^\mu < 0$  or  $\delta_i^\mu > 0$ . Thus *strongly lensed images generated at a saddle point tend to be demagnified/magnified by intervening massive halos if  $1 - \kappa_i > 0 (< 0)$ .*

It is worthwhile to note that the mass-sheet degeneracy can be broken if intervening halos affect the fluxes of multiply lensed images significantly. For instance, under a transformation with a constant scalar  $\lambda$  in the background convergence and shear  $1 - \kappa_i \rightarrow \lambda(1 - \kappa_i) = 1 - \kappa_i'$  and  $\gamma_i \rightarrow \lambda\gamma_i = \gamma_i'$ , which preserves the positions of a lensed images of a point source by changing the position at the source plane as  $\mathbf{y} \rightarrow \lambda\mathbf{y}$ . However, the magnification contrast  $\delta_i^\mu$  depends on  $\lambda$  as  $\delta_i^\mu \propto \lambda^{-1}$  for  $|\delta_i^\mu| \ll 1$ . Therefore, from observed  $\delta_i^\mu$ , one would be able to put a constraint on  $\lambda$  if  $\delta\kappa$  and  $\delta\gamma_1$  could be measured with shifts of positions of extended images due to intervening halos (Inoue & Chiba 2005a,b; Vegetti et al. 2012).

In order to quantify anomalies in flux ratios of a lens system with quadruple images, the cusp-caustic relation has been used in literature. In the positive cusp case, for close three adjacent bright images (A, B and C) with magnifications  $\mu_A, \mu_B$  and  $\mu_C$ , and the opening angle  $\theta$  spanned by the center of two images in the ends and the lens center, the relation is

$$R_{cusp} \equiv \frac{|\mu_A + \mu_B + \mu_C|}{|\mu_A| + |\mu_B| + |\mu_C|} \rightarrow 0, \quad (17)$$

where  $|\mu_A| + |\mu_B| + |\mu_C| \rightarrow \infty$  and  $\theta \rightarrow 0$ . However, in practice, none of observed quadruple image systems satisfy this asymptotic condition. For instance, the observed smallest opening angle is  $\Delta\theta \sim 30^\circ$ . Most radio or MIR quadruple image systems have even larger opening angles  $\Delta\theta \sim 100^\circ$ . Furthermore, the potential of the primary lens is sometimes not smooth. For example, luminous dwarf galaxies, or groups of galaxies in the neighborhood of quadruple images can significantly alter the flux ratios. In fact, some lens systems with anomalies in the flux ratios may consist of multiple lenses. Although  $R_{cusp}$  is suitable for ideal systems with  $|\mu_A| + |\mu_B| + |\mu_C| \rightarrow \infty$  and  $\Delta\theta \sim 0$ , it may not be suitable for most of observed quadruple-image systems.

To circumvent this problem, we introduce a new estimator

$$\eta^2 \equiv \frac{1}{2N_c} \sum_{i \neq j} \left[ \delta_i^\mu - \delta_j^\mu(\text{saddle}, \kappa_j < 1) \right]^2, \quad (18)$$

where  $\delta_i^\mu$  denotes a magnification contrast for an image  $i$  with a positive parity or a negative parity with  $\kappa_i > 1$  and  $\delta_j^\mu(\text{saddle}, \kappa_j < 1)$  is a magnification contrast for an image  $j$  that has a negative parity with  $\kappa_j < 1$ . Here  $N_c$  is the

total number of combination  $i \neq j$  in the summation. Magnification for an unperturbed system is given by a best-fit model based on positions of images and the center of the primary lens galaxy. Therefore,  $\eta$  is not a directly observable quantity. Roughly speaking,  $\eta$  corresponds to a mean magnification contrast per image due to clustering halos in the line-of-sight. Note that  $\eta$  depends on only observed and modeled flux ratios provided that the magnification perturbations are sufficiently small. Here we put a negative sign before  $\delta_j^\mu(\text{saddle}, \kappa_j < 1)$  because for systems with significant contribution from intervening halos, we expect demagnification for saddle points with  $\kappa < 1$ , namely,  $\langle \delta_j^\mu \rangle < 0$  as we have seen. Suppose we have a set of images with two minima, A and C and one saddle B with  $\kappa_B < 1$ . Then the estimator of flux-ratio anomalies can be written as

$$\eta^2(\text{A,B,C}) = \frac{1}{4} [(\delta_A^\mu - \delta_B^\mu)^2 + (\delta_C^\mu - \delta_B^\mu)^2]. \quad (19)$$

In terms of observed fluxes  $A, B, C$  and estimated unperturbed fluxes  $A_0, B_0, C_0$ , the estimator is approximately given by observed flux ratios,

$$\eta^2 \approx \frac{1}{4} \left[ \left( \frac{AB_0}{A_0B} - 1 \right)^2 + \left( \frac{CB_0}{C_0B} - 1 \right)^2 \right]. \quad (20)$$

In a similar manner, for four-image system with two minima A and C and two saddles B and D with  $\kappa < 1$ , the estimator is

$$\begin{aligned} \eta^2(\text{A,B,C,D}) &= \frac{1}{8} [(\delta_A^\mu - \delta_B^\mu)^2 + (\delta_C^\mu - \delta_B^\mu)^2 \\ &+ (\delta_A^\mu - \delta_D^\mu)^2 + (\delta_C^\mu - \delta_D^\mu)^2]. \end{aligned} \quad (21)$$

### 3 CONSTRAINED CONVERGENCE POWER

We consider strong lens systems in which positions of multiple images are well fit by the potential of the primary lens that consists of either a single or multiple lenses with a smooth potential though the image flux ratios do not necessarily agree with the model prediction. In these systems, perturbation of image shifts due to other massive halos or voids in the neighborhoods of lensed images should be sufficiently small. This can be interpreted as an observational selection bias that no other dark massive halos or voids do not reside in the neighborhoods of line-of-sight of images since presence of these objects would otherwise perturb the positions of images and lenses significantly. Moreover, modeling the primary lens galaxies and neighboring groups or clusters would also induce an observational selection bias. The two-point correlation of matter density field in the line-of-sight constrained by these selection biases are determined by the best-fitting accuracy in position of images and lenses as follows.

Suppose that positions of a pair of multiple images A and B with angular coordinates  $\theta_A$  and  $\theta_B$  separated by an angle  $\theta_{AB}$  are fit by a smooth lens model within an error  $\epsilon$ . This implies that total angular shifts  $\delta\theta$  of image A and B due to intervening halos or voids in the line-of-sight should satisfy (see Fig.1)

$$|\delta\theta(\theta_A) - \delta\theta(\theta_A + \theta_{AB})| < \epsilon. \quad (22)$$

Assuming statistical isotropy and homogeneity for background perturbations, equation (22) gives

$$2\langle \delta\theta^2(0) \rangle - 2\langle \delta\theta(0)\delta\theta(\theta_{AB}) \rangle < \epsilon^2, \quad (23)$$

where  $\langle \rangle$  denotes an ensemble average.

Using Limber's approximation, a 2-point correlation function of astrometric shifts  $\delta\theta$  for a pair of light rays separated by an angle  $\theta$  can be written in terms of matter power spectrum  $P_\delta(k; r)$ , comoving distance to the source  $r_S$ , redshift  $z(r)$  as (Bartelmann & Schneider 2001)

$$\begin{aligned} \xi_{\delta\theta}(\theta) &\equiv \langle \delta\theta(0)\delta\theta(\theta) \rangle \\ &= \frac{9H_0^4\Omega_{m,0}^2}{c^4} \int_0^{r_S} dr \left( \frac{r-r_S}{r_S} \right)^2 [1+z(r)]^2 \\ &\times \int_0^\infty \frac{dk}{2\pi k} W(k; k_{cut}(r)) P_\delta(k; r) J_0(g(r)k\theta), \end{aligned} \quad (24)$$

where

$$g(r) = \begin{cases} r, & r < r_L \\ \frac{r_L(r_S-r)}{r_S-r_L}, & r \geq r_L \end{cases} \quad (25)$$

describes the trajectory of photons that pass through a primary lens at comoving distance  $r = r_L$ ,  $J_0$  is the zeroth-order Bessel function, and  $W(k; k_{cut}(r))$  denotes the window function in which modes with wavenumber  $k$  smaller than  $k_{cut}(r)$  at comoving distance  $r - dr/2 < r < r + dr/2$  are significantly suppressed. We will discuss the property of  $W(k; k_{cut}(r))$  in detail in next section. From equations (23), (24), and (25), one obtains the cutoff scale  $k_{cut}$  as a function of  $\epsilon$  and  $r$ . Because the accuracy in position fitting is generally far better than that of flux ratios in observations, it may still allow deviation in flux ratios due to constrained convergence and shear fields in the line-of-sight. The constrained 2-point correlation of convergence  $\kappa$  as a function of a separation angle  $\theta$  is

$$\begin{aligned} \xi_\kappa(\theta) &\equiv \langle \delta\kappa(0)\delta\kappa(\theta) \rangle \\ &= \frac{9H_0^4\Omega_{m,0}^2}{4c^4} \int_0^{r_S} dr r^2 \left( \frac{r-r_S}{r_S} \right)^2 [1+z(r)]^2 \\ &\times \int_0^\infty \frac{dk}{2\pi} k W(k; k_{cut}(r; \epsilon)) P_\delta(k; r) J_0(g(r)k\theta), \end{aligned} \quad (26)$$

where  $g(r)$  is given by (25). At small angular scales  $l \gg 1$ , the constrained convergence power is given by a Hankel transform of equation (26)

$$P_\kappa(l) = 2\pi \int d\theta \theta \xi_\kappa(\theta) J_0(\theta l). \quad (27)$$

In terms of obtained constrained convergence correlation function  $\xi_\kappa$ , one can estimate an ensemble average of the estimator  $\eta^2$  defined in the previous section, which measures anomaly in flux ratios. For example, for three images with two minima A and C and one saddle B with  $\kappa_B < 1$ , using an approximation (11), for  $|\delta_i^\mu| \ll 1$ , an ensemble average of the estimator (19) can be written as

$$\begin{aligned} \langle \eta^2 \rangle &= \frac{1}{4} \left[ (J_A + J_B)\sigma_\kappa^2(0) - 2J_{AB}\xi_\kappa(\theta_{AB}) \right. \\ &\quad \left. + (J_B + J_C)\sigma_\kappa^2(0) - 2J_{BC}\xi_\kappa(\theta_{BC}) \right], \end{aligned} \quad (28)$$

where

$$J_i = \mu_i^2(4(1-\kappa_i)^2 + 2\gamma_i^2), \quad (29)$$

and

$$J_{ij} = \mu_i\mu_j(4(1-\kappa_i)(1-\kappa_j) + 2\gamma_i\gamma_j), \quad (30)$$

for  $i = A, B, C$  and  $\gamma_i = (\gamma_{i1}^2 + \gamma_{i2}^2)^{1/2}$ . Here  $\sigma_\kappa(0) \equiv \sqrt{\xi_\kappa(0)}$ . In deriving equation (30), we have used a well known fact that  $\xi_\kappa(\theta) = 2\xi_{\gamma_\alpha}(\theta)$  and  $\langle \delta\gamma_1\delta\gamma_2 \rangle = \langle \delta\kappa\delta\gamma_\alpha \rangle = 0$ , for  $\alpha = 1, 2$  provided that background matter density fluctuations are statistically homogeneous and isotropic. In a similar manner, for a four-image system with two minima A and C and two saddles B and D with  $\kappa < 1$ , an ensemble average of the estimator  $\eta^2(A, B, C, D)$  is given by

$$\begin{aligned} \langle \eta^2 \rangle &= \frac{1}{8} \left[ (J_A + J_B)\sigma_\kappa^2(0) - 2J_{AB}\xi_\kappa(\theta_{AB}) \right. \\ &\quad + (J_C + J_D)\sigma_\kappa^2(0) - 2J_{CD}\xi_\kappa(\theta_{CD}) \\ &\quad + (J_A + J_D)\sigma_\kappa^2(0) - 2J_{AD}\xi_\kappa(\theta_{AD}) \\ &\quad \left. + (J_B + J_C)\sigma_\kappa^2(0) - 2J_{BC}\xi_\kappa(\theta_{BC}) \right], \end{aligned} \quad (31)$$

where  $J_i$  and  $J_{ij}$  are given by (29) and (30). Application of these statistics to mid-infrared lenses is presented in section 6.

## 4 NON-LINEAR POWER SPECTRUM

In order to evaluate equations (24) and (26), we need an accurate matter power spectrum at scales down to  $k^{-1} = O[1] h^{-1}$  kpc. However, analytical fitting formulae in literature are not suitable for this purpose. For example, the halo-fit model by Smith et al. (2003) has been frequently used to evaluate the non-linear power spectrum  $P(k)$ . However, as shown by several authors (see e.g. Takahashi et al. (2012)) it was shown that this model underestimates the power spectrum by some tens percent than the latest cosmological simulation results on small scales  $k \gtrsim 1 h\text{Mpc}^{-1}$ . Hence, in this study, we run cosmological  $N$ -body simulations to investigate the non-linear power spectrum  $P(k)$  at galactic scales and we make a new fitting formula of  $P(k)$ . For simplicity, however, we do not input baryon in our simulation.

In our cosmological  $N$ -body simulation, we use a cubic box with a comoving side length of  $10 h^{-1}$  Mpc with  $N_p^3 = 1024^3$  and  $512^3$  collisionless particles. We can check a numerical convergence of our simulation by comparing a low resolution simulation ( $N_p^3 = 512^3$ ) with a high resolution one ( $1024^3$ ). The softening comoving length is fixed to be 2.5% of the mean particle separation, corresponding to  $0.25(0.5) h^{-1}$  kpc for  $N_p^3 = 1024^3(512^3)$ . The particle mass is  $7.1 \times 10^4(5.7 \times 10^5) h^{-1} M_\odot$  for  $1024^3(512^3)$  collisionless particles. Therefore, the minimum mass of halos resolved by our simulations is  $1.4 \times 10^5 h^{-1} M_\odot$  (corresponding to 20 particles).

We use a simulation code called Gadget2 (Springel et al. 2001; Springel 2005). We calculate the initial conditions of particles based on the second-order Lagrangian perturbation theory (2LPT) (Crocco et al. 2006; Nishimichi et al. 2009) with the initial linear power spectrum obtained by Eisenstein & Hu (1999). The initial redshift of our simulations is  $z_{\text{in}} = 99$  and we dump the simulation results of the particle positions at  $z = 0 - 4$ . We prepare two independent realizations for  $N_p^3 = 512^3$  at

$z = 0, 0.35, 0.7, 1, 1.5, 2.2, 3, 4$  and a single realization for  $N_p^3 = 1024^3$  at  $z = 0.35, 0.7, 1, 1.5, 2.2, 3, 4$ . In calculating the power spectrum  $P(k)$ , we assign the particles on  $N_g^3 = 1280^3$  grid using the cloud-in-cell (CIC) method to obtain density fluctuations. After performing the Fourier transform, we correct the window function of CIC as  $\tilde{\delta}_{\mathbf{k}} \rightarrow \prod_{i=x,y,z} [\text{sinc}(Lk_i/2N_g)]^2 \times \tilde{\delta}_{\mathbf{k}}$ , where  $\tilde{\delta}_{\mathbf{k}}$  is the density fluctuation in the Fourier space (Hockney & Eastwood 1988). In addition, to evaluate the power spectrum on small scales accurately, we fold the particle positions  $\mathbf{x}$  into a smaller box by replacing  $\mathbf{x} \rightarrow \mathbf{x}\% (L/2^n)$  where the operation  $a\%b$  gives the remainder of the division of  $a$  by  $b$  (e.g. Valageas & Nishimichi (2011)). Then, the resolution becomes effectively  $2^n$  times finer. Here we use  $n = 2$  and 4. Finally, we evaluate the power spectrum:

$$P(k) = \sum_k \frac{1}{N_k} |\tilde{\delta}_{\mathbf{k}}|^2, \quad (32)$$

where the summation is done from  $k - \Delta k/2$  to  $k + \Delta k/2$  with a binwidth  $\Delta k$ , and  $N_k$  is the number of mode in the bin. We use a logarithmic binwidth,  $\Delta \log_{10}(k/h\text{Mpc}^{-1}) = 0.05$ . For our polynomial fitting, we do not use the  $P(k)$  at small scales where the shot noise begin to dominate the signal. The Nyquist wave number determined by the mean particle separation is  $k_{\text{Nyq}} = (2\pi/L)(N_p/2)$ , which corresponds to  $k_{\text{Nyq}} = 320(160) h\text{Mpc}^{-1}$  for  $N_p^3 = 1024^3(512^3)$  particles with  $L = 10h^{-1}\text{Mpc}$ . Hence, we can probe the density fluctuations on very small scales,  $k = 320 h\text{Mpc}^{-1}$ . We have checked that the power spectra  $P(k)$  of our  $N$ -body simulations agree with simulations with higher resolution in which we use finer simulation parameters of the time steps, force calculation, etc. within 2(6%) for  $k < 100(320) h\text{Mpc}^{-1}$ .

We also use simulation results by Takahashi et al. (2012). They use the same codes as ours (Gadget2 and 2LTP initial condition) and employ  $1024^3$  particles in the simulation boxes of  $L = 2000, 800, 320 h^{-1} \text{Mpc}$  and combined the  $P(k)$  on the different box sizes to cover a wide range of scales. They provide the  $P(k)$  up to  $k = 30 h\text{Mpc}^{-1}$  at  $z = 0 - 10$ . Hence we use their result for  $k < 30 h\text{Mpc}^{-1}$  and the present result for  $k > 30 h\text{Mpc}^{-1}$ .

As one can clearly see in Fig. 2, the power spectra of our simulations at scales  $k > 30 h\text{Mpc}^{-1}$  are significantly larger than the values predicted in the original halo-fit model (Smith et al. 2003). At scales  $k \sim 300 h\text{Mpc}^{-1}$  which are relevant to the weak lensing effect of line-of-sight halos, our fitting formula, which improves the original halo-fit model down to  $k \sim 300 h\text{Mpc}^{-1}$  (see Appendix for details) predicts a factor of 2–3 enhancement in amplitude of the dimensionless power  $\Delta(k) = \sqrt{\Delta^2(k)}$  at redshifts  $0 < z < 2$ . As we shall see in the following sections, this enhancement plays an important role in explaining the origin of anomalies in flux ratios.

The suppression of power spectra  $P(k)$  predicted by our simulation at scales smaller than the Nyquist frequency is due to the lack of resolution. In fact, the power spectra  $P(k)$  in simulations with  $1024^3$  particles are systematically larger than those simulated with  $512^3$  particles at  $k > 100 h\text{Mpc}^{-1}$ . In what follows, however, we use our new fitting formula to estimate the power spectra at very small scales  $k > 320 h\text{Mpc}^{-1}$ . Although the accuracy is not guaranteed, it may give a good approximation on very small

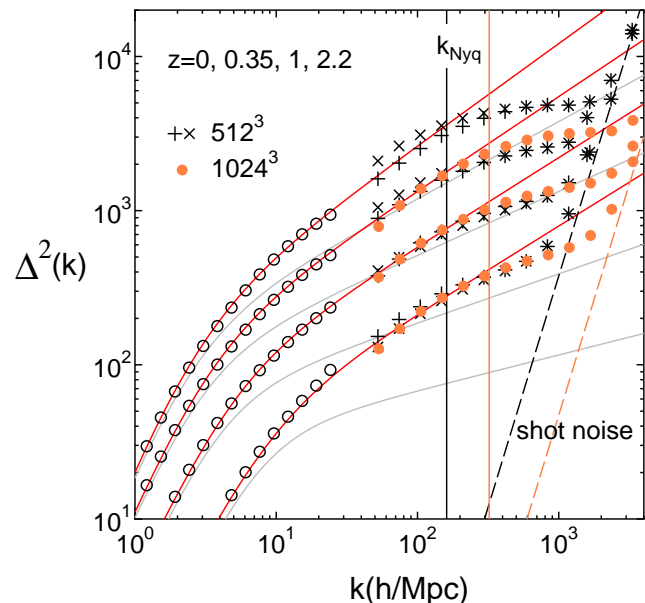


**Figure 2.** Plots of dimensionless power spectra,  $\Delta^2(k) = k^3 P(k)/(2\pi^2)$ , at  $z = 0, 0.35, 1$  and  $2.2$  (from top to bottom). Our simulation results of  $L = 10 h^{-1}\text{Mpc}$  box with  $512^3$  particles are plotted as plus and cross symbols, corresponding to two independent realizations. Our simulation results of  $L = 10 h^{-1}\text{Mpc}$  box with  $1024^3$  particles and those by Takahashi et al. (2012), which match our simulation results at  $k = 30 h\text{Mpc}^{-1}$  are plotted as filled circles and empty circles, respectively. Our fitting functions (see Appendix) and the predicted values in the halo-fit model (Smith et al. 2003) are plotted as solid curves in red and gray, respectively. The vertical and dashed lines represent the Nyquist wave numbers  $k_{\text{Nyq}}$  and the shot noises for  $N_p^3 = 1024^3$  (right) and  $512^3$  (left), respectively.

scales since the power tends to increase as the resolution becomes higher.

Assuming that the comoving size  $r$  of a density fluctuation is  $r \sim \pi/k$ , the relation between a mass scale of clustering non-linear halos and the wavenumber can be given by

$$M(k; z) \sim \frac{4\pi^4}{3k^3} \sqrt{\Delta^2(k)} \rho(z), \quad (33)$$

where  $\rho(z)$  is a mean comoving matter density of the background universe at redshift  $z$ . As shown in Fig. 3, for a given wavenumber  $k$ , the corresponding mass  $M$  increases as the redshift  $z$  increases due to time evolution of the fluctuations. We find that a wavenumber that corresponds to the Nyquist frequency  $k_{\text{Nyq}} = 320 h\text{Mpc}^{-1}$  corresponds to  $M = 3 \times 10^7 M_\odot$  at  $z = 0$ .  $k = 1000 h\text{Mpc}^{-1}$ ,  $10000 h\text{Mpc}^{-1}$  corresponds to  $M = 1 \times 10^6 M_\odot$ ,  $3 \times 10^3 M_\odot$  at  $z = 0$ , respectively.

## 5 SEMI-ANALYTIC ESTIMATE

Based on formalism developed in section 2 and 3, we can estimate the deflection and flux change of strongly lensed

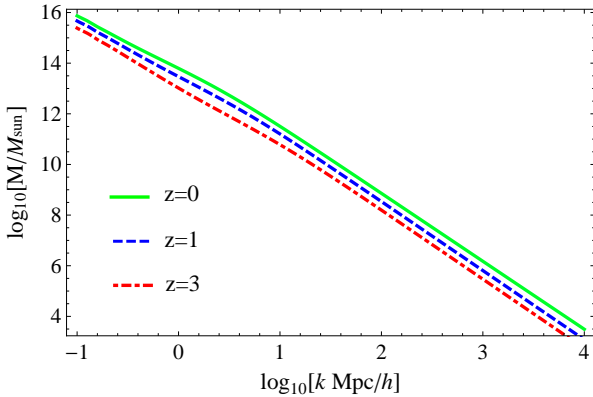


**Figure 3.** Approximated relation between mass  $M$  and a wavenumber  $k$  for non-linear matter fluctuations at redshift  $z = 0$  (full),  $z = 1$  (dashed), and  $z = 3$  (dot-dashed).

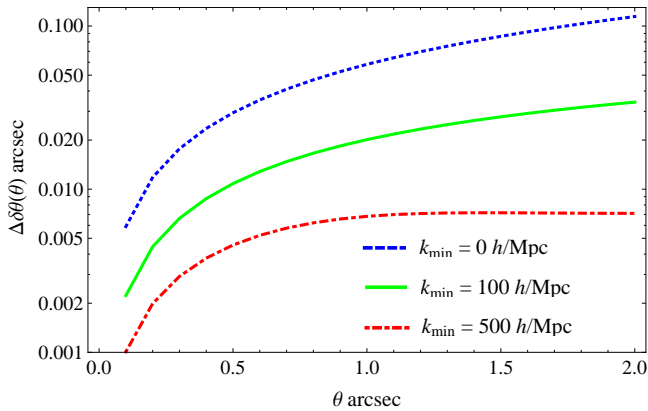


**Figure 4.** Rms value of difference in shifts of image position  $\Delta\delta\theta$  as a function of a separation angle  $\theta$  for minimum wavenumber  $k_{min} = 0 h\text{Mpc}^{-1}$  (dashed),  $100 h\text{Mpc}^{-1}$  (full),  $500 h\text{Mpc}^{-1}$  (dot-dashed). Source and lens redshifts are  $z_S = 3$ ,  $z_L = 0.5$ , respectively. The upper limit of the wavenumber is assumed to be  $k_{max} = 1000 h\text{Mpc}^{-1}$ .

images using the non-linear matter power spectrum obtained in section 4. Firstly, we calculate the rms of difference in the total angular shifts  $\delta\theta$  between two images separated by  $\theta$ ,

$$\Delta\delta\theta(\theta) \equiv [(\delta\theta(\theta) - \delta\theta(0))^2]^{1/2}. \quad (34)$$

In order to study the dependence on the scale of matter fluctuation in the line-of-sight, for simplicity, we adopt a “sharp k-space” window function,

$$W_s(k; k_{cut}) \equiv \begin{cases} 0, & k < k_{min} \\ 1, & k \geq k_{min} \end{cases} \quad (35)$$

for which modes  $k < k_{min} = k_{cut}$  are cut off in equation (24). As shown in Fig. 4, for  $k_{min} < 100 h\text{Mpc}^{-1}$ , the difference in the image shift  $\Delta\delta\theta$  becomes larger as the separation angle increases. However, for  $k_{min} = 500 h\text{Mpc}^{-1}$ ,  $\Delta\delta\theta$  has

a peak around  $\theta = 1.5$  arcsec and it gradually decreases as  $\theta$  increases due to a cutoff at small scales  $k > k_{max}$ . For a given separation angle,  $\Delta\delta\theta$  gets smaller as  $k_{min}$  increases.

Without any cutoff in the background fluctuations, it turns out that the difference in the shifts is  $\Delta\delta\theta \sim 0.06$  arcsec for  $k_{max} = 1000 h\text{Mpc}^{-1}$  and separation angle  $\theta = 1$  arcsec, which is the typical scale of the Einstein radius of a primary lens. This is significantly larger than the observed error  $\epsilon$  of relative positions of light centers, which is of the order of 1 mas for most quadruple image lenses observed in the optical or radio band. This is because contribution from modes with wavenumber  $k < k_{min} = O[10^{2-3}]h\text{Mpc}^{-1}$  is already taken into account in the fitted model, including neighboring clusters, groups, massive galaxy halos and luminous dwarf galaxy halos provided that the position of modeled images and the center of the primary lens agree with the observed values. In fact, as shown in Fig. 5 on angular scales smaller than 1 arcsec, the largest contribution comes from modes on scales  $k \sim 10 h\text{Mpc}^{-1}$  at which the one-halo term begins to dominate the matter power spectrum in the halo fitting model. For larger separation angles  $\theta > 1$  arcsec, relative contribution from smaller scale fluctuations decreases. If the residual difference in the position of lensed images is less than the rms value, then contribution from clustering halos on such scales should be negligible. As we can see in Fig. 6, if the cutoff scale  $k_{min}$  is constant as a function of redshift as we have assumed, then the dominant contribution comes from fluctuations near the lens plane at  $z \sim z_L$  in the line-of-sight. This can be understood as a result of two effects: (i) The lensing weight function  $(r - r_S)(1 + z(r))$  for astrometric shifts in the integrand of equation (24) is maximum at around a half comoving distance to the source, and vanishes at  $r = r_S$ . (ii) Because of convergence of photon trajectories toward a point-like source beyond the lens plane, the relevant comoving scale of fluctuations becomes smaller, which leads to a suppression of the contribution. The latter effect (ii) becomes more significant as a cutoff scale becomes larger and the lens redshift  $z_L$  becomes smaller.

Thus we interpret that the contribution from fluctuations on scale  $k \sim 10 h\text{Mpc}^{-1}$  at  $z \sim z_L$  correspond to a primary lens galaxy or luminous galaxies around the primary lens. If large-angle fluctuations of projected gravitational potential in the line-of-sight of multiply lensed images have been modeled as an external shear ( $m = 2$ ) or low multipole terms ( $m = 3$ ), which corresponds to contribution from clusters or groups of galaxies, we would only need to take into account small scale fluctuations with wavenumbers  $k \gtrsim k_{cut}$  where  $k_{cut}$  is roughly equivalent to the scale of observable luminous dwarf galaxies at the lens plane. These small scale fluctuations may affect the flux ratios significantly if the total perturbations of convergence integrated in the line-of-sight is sufficiently large.

In order to assess the effects of small scale fluctuations on the flux ratios, we consider rms of the self correlation of convergence  $\sigma_\kappa(0) = \sqrt{\xi_\kappa(0)}$  as a function of source redshift  $z_S$ . We can see in Fig. 7 that contribution of small scale fluctuations ranging from  $k_{min} \sim O(10^2)h\text{Mpc}^{-1}$  to  $k_{max} = 1000 h\text{Mpc}^{-1}$  would yields  $\sigma_\kappa(0) \sim 0.01$  in convergence if the source redshift satisfies  $z_S \gtrsim 3^1$ . In other words,

<sup>1</sup> If we consider contribution from modes with wavenumber

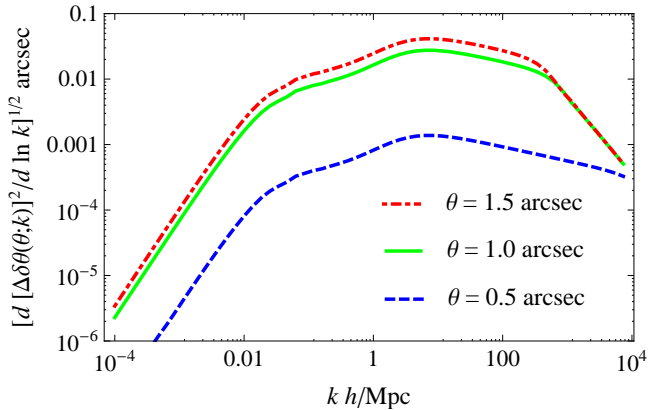


**Figure 5.** Contribution of each mode to  $\Delta\delta\theta$  marginalized over redshift  $z$  as a function of wavenumber  $k$ . For separation angle  $\theta \sim 1$ , major contribution to  $\Delta\delta\theta$  comes from modes  $k \sim 10 h\text{Mpc}^{-1}$ . Plotted curves are for separation angle  $\theta = 0.5''$  (dashed),  $1.0''$  (full),  $1.5''$  (dot-dashed) with source redshift  $z_S = 3$  and lens redshift  $z_L = 0.5$ . We assume  $k_{max} = 10000 h\text{Mpc}^{-1}$ .

the surface density in small scale structures in line-of-sight is of the order of one percent of that of the primary lens. This may be too small to be of any importance. However, as we have seen in section 3, *anomaly in the flux ratio is proportional to the magnification of the primary lens*, i.e.,  $\eta \sim 2(\mu)\sigma_\kappa(0)$  where  $\mu$  is the mean magnification of images provided that  $\kappa \sim \gamma \sim 0.5$  and correlations between different images are negligible. For an image with modest magnification  $\mu \sim 5$ , it would yield 10 per cent change in flux ratios,  $\eta \sim 0.1$  if  $z_S \sim 3$ . Such a change is sufficient to explain the order of observed anomalies (Metcalf 2005a,b). Moreover, if we take into account the correlation of convergence between different images, anomaly in flux ratios can be more distinctive. As we can see in Fig. 8, for a separation angle  $\theta \sim 0.5$  arcsec, the amplitude of 2-point correlation  $\xi_\kappa(\theta)$  is still comparable to the self correlation  $\sigma_\kappa^2(0)$ . Therefore, we expect less significant anomaly in the flux ratios for systems with larger Einstein radius as long as accuracy in position fitting does not change. In other words, if such an anomaly is observed in the primary lens with large separation angles, the chance of significant perturbation to one of the lensed images is higher than the cases in which all the images are perturbed at the same time at similar levels.

As is the case of shifts of image positions, the largest contribution to the amplitude of convergence  $\sigma_\kappa(0)$  comes from modes on scales  $k \sim 10 h\text{Mpc}^{-1}$  at approximately a half distance to the source (Fig. 9). If we consider a sharp k-space filter with  $k_{cut} = k_{min}$ , then the small scale contribution to the convergence  $\sigma_\kappa(0)$  is smaller than contribution from modes with  $k \sim k_{min}$ . In other words, the largest contribution to the amplitude of convergence  $\sigma_\kappa(0)$  comes from fluctuations with wavenumber  $k \sim k_{min}$  at approximately a half distance to the source. Therefore, we consider

$k > 1000 h\text{Mpc}^{-1}$ , the rms convergence  $\sigma_\kappa(0)$  can be further increased. See also Fig. 9.

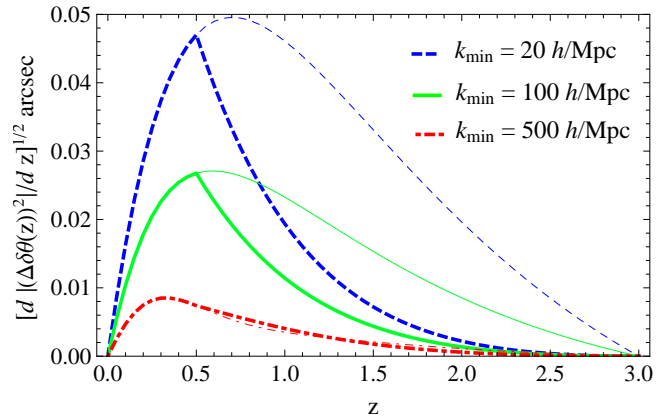


**Figure 6.** Contribution of fluctuations on different planes at redshift  $z$  to  $\Delta\delta\theta$  marginalized over wavenumber  $k$ . Plotted curves are for minimum wavenumber  $k_{min} = 20 h\text{Mpc}^{-1}$  (dashed),  $100 h\text{Mpc}^{-1}$  (full), and  $500 h\text{Mpc}^{-1}$  (dot-dashed). Thick and thin curves correspond to lens redshifts  $z_L = 0.5$  and  $z_L = 2.99$ , respectively. We assume source redshift  $z_S = 3$ , separation angle  $\theta = 1$  arcsec, and the upper limit of the wavenumber  $k_{max} = 1000 h\text{Mpc}^{-1}$ .

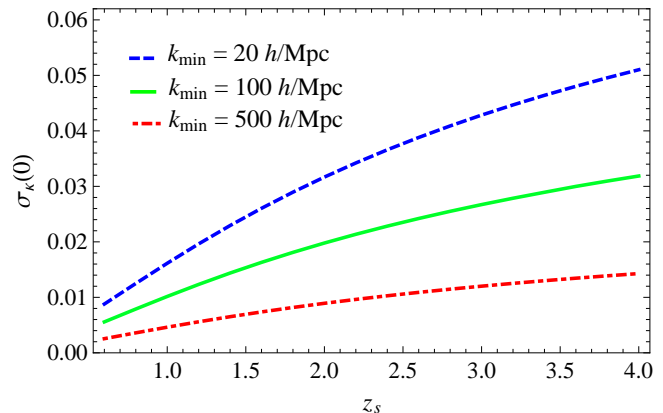


**Figure 7.** Self correlation of convergence as a function of source redshift  $z_S$ . Plotted curves are for minimum wavenumber  $k_{min} = 20 h\text{Mpc}^{-1}$  (dashed),  $100 h\text{Mpc}^{-1}$  (full), and  $500 h\text{Mpc}^{-1}$  (dot-dashed). We assume lens redshift is  $z_L = 0.5$  and the upper limit of the wavenumber is  $k_{max} = 1000 h\text{Mpc}^{-1}$ .

that influence of redshift dependence of filtering functions  $W(k; k_{cut}(z))$  on  $\sigma_\kappa(0)$  is small.

So far we have considered the “sharp k-space” filter for cutting off the contribution from large scale fluctuations with  $k < k_{min}$ . However, in real setting, large scale fluctuations in the line-of-sight are removed in real space as components that yield an external shear and a constant convergence or distort the relative positions of the lensed images and the lens centroid. Therefore, contributions from modes  $k < k_{min}$  may not be negligible. In other words, more mas-



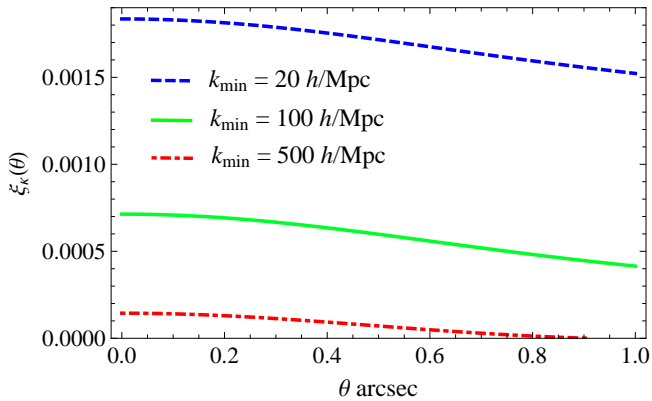


**Figure 8.** 2-point correlation of convergence as a function of separation angle  $\theta$  between two images. The three curves are for  $k_{\min} = 20 \text{ hMpc}^{-1}$  (dashed),  $100 \text{ hMpc}^{-1}$  (full), and  $500 \text{ hMpc}^{-1}$  (dot-dashed). We assume lens redshift  $z_L = 0.5$ , source redshift  $z_S = 3$ , and the upper limit of the wavenumber  $k_{\max} = 1000 \text{ hMpc}^{-1}$ .

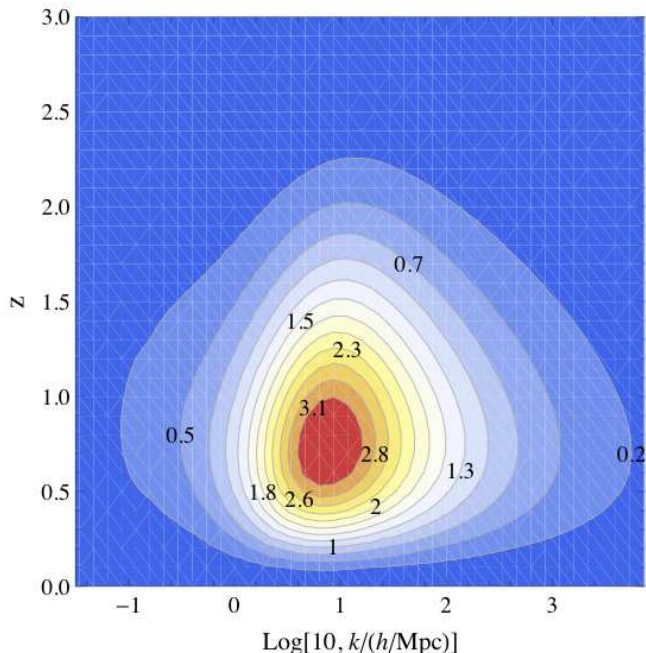


**Figure 9.** Contour plots of  $\partial^2 \sigma_\kappa^2(0)/\partial z \partial \ln k$ . We assume lens redshift  $z_L = 0.5$ , source redshift  $z_S = 3$ , and the upper limit of the wavenumber  $k_{\max} = 10000 \text{ hMpc}^{-1}$ .

sive objects placed near the line-of-sight could affect the flux ratios. In order to assess this effect, we consider a ‘‘Gaussian’’ filter that is defined as an integration of the Gaussian distribution function as

$$W_g(k; k_{\text{cut}}) \equiv \frac{1}{2} \left[ 1 + \text{Erf} \left( \frac{\log_{10}(k/k_{\text{cut}})}{\sqrt{2} \log_{10}(1+q)} \right) \right], \quad (36)$$

where Erf is the error function and  $q$  describes the width of the filter  $\Delta \log_{10} k \sim q$ . There should be an upper limit for  $q$  as the perturber in the line-of-sight is too massive, it becomes observable near the primary lens. As a reasonable guess, we consider two types of the ‘‘Gaussian’’ filter,  $q = 0.4$  and  $q = 0.9$ . Approximately 4 times massive objects are included for  $q = 0.4$  and 20 times massive for  $q = 0.9$  (Fig. 10). We choose two types of ‘‘UV’’ cutoff,  $k_{\max} = 1000 \text{ hMpc}^{-1}$  and  $k_{\max} = 10000 \text{ hMpc}^{-1}$ . The latter scale gives an Einstein radius  $O[1 \text{ pc}]$  at cosmological scales if the fluctuations of corresponding mass scales  $\sim 10^3 M_\odot$  form point masses.

For a given maximally allowed shift  $\epsilon = \Delta \delta \theta (\theta = 1'')$ ,  $k_{\text{cut}}$  is obtained from equations (24) and (25) for each filter. Then we calculate the 2-point correlation function of convergence  $\xi_\kappa$ . We adopt separation angles between an image and a lens  $\theta = 0'', 0.5'',$  and  $1''$  as typical examples. As shown in Fig. 11, the differences between different types of filters are astonishingly small for  $\theta = 0.5''$ . For  $\theta = 0, 1''$ , the relative difference in  $\xi_\kappa$  is at most 35 per cent. Therefore, the effect of large scale fluctuations with  $k < k_{\text{cut}}$  to  $\eta$  is less than  $\sim 20$  per cent. It should be noted, however, that for  $\theta = 0''$ , amplitude of  $\xi_\kappa$  is systematically reduced if contribution from large scale fluctuations is taken into account. This can be explained as follows. At  $\theta \sim 0''$ , the ratio between contributions to the shift  $\Delta \delta$  from large scales  $k < k_{\text{cut}}$  and small scales  $k > k_{\text{cut}}$  is *smaller* than the ratio between contributions to the convergence  $\xi_\kappa$  from large scales  $k < k_{\text{cut}}$  and small scales  $k > k_{\text{cut}}$ . In other words, the contributions to the 2-point correlation of convergence is a steeper function of  $k$  in comparison with the contribution to the shift  $\Delta \delta \theta$  (see Fig. 5 and Fig. 9). As the function form of the filter function is common for the both quantities, the above relation yields a further reduction in the 2-point correlation  $\xi_\kappa$  if the cut off scale is determined from the shift  $\Delta \delta \theta$ . At  $\theta = 1''$ , on the other hand, the ratio between contributions to the shift  $\Delta \delta$  from large scales  $k < k_{\text{cut}}$  and small scales  $k > k_{\text{cut}}$  is *larger* than the ratio between contributions to the convergence  $\xi_\kappa$  from large scales  $k < k_{\text{cut}}$  and small scales  $k > k_{\text{cut}}$ . This yields an enhancement of 2-point correlation function  $\xi_\kappa$ . If  $q > 0.9$ , we expect that the predicted  $\eta$  will be much smaller.

## 6 MIR QSO-GALAXY QUADRUPLE LENSES

In what follows, we only use MIR data for flux of gravitationally lensed QSOs with quadruple images (see table 1). The number of lensed images used in analysis of flux ratios is denoted as  $N$ . We discard any data with small signal-to-noise ratio in the MIR fluxes. Relative positions of macro-lensed images and the lensing galaxy are taken from the CfA-Arizona Space Telescope Lens Survey (CASTLES)<sup>2</sup> in the visible and near-IR bands except for H1413+117.

For four-image lenses, the mean error in the image separation between a lensed image and a position of the centroid of the primary lens is denoted as  $\langle \epsilon \rangle$ . We assume that the errors of image positions or a centroid of lensing galaxy are not correlated each other and the errors in image separation obey Gaussian distributions. Although constraint on contribution from intervening halos is most stringent for a

<sup>2</sup> See <http://www.cfa.harvard.edu/castles/>

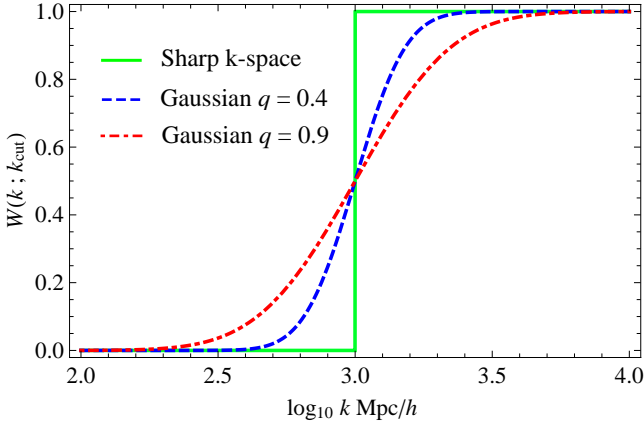


**Figure 10.** The “Gaussian” filters with  $q = 0.4$  (dashed curve)  $q = 0.9$  (dot-dashed curve) and the sharp k-space filter (full curve). We assume  $k_{cut} = 1000 h\text{Mpc}^{-1}$ .

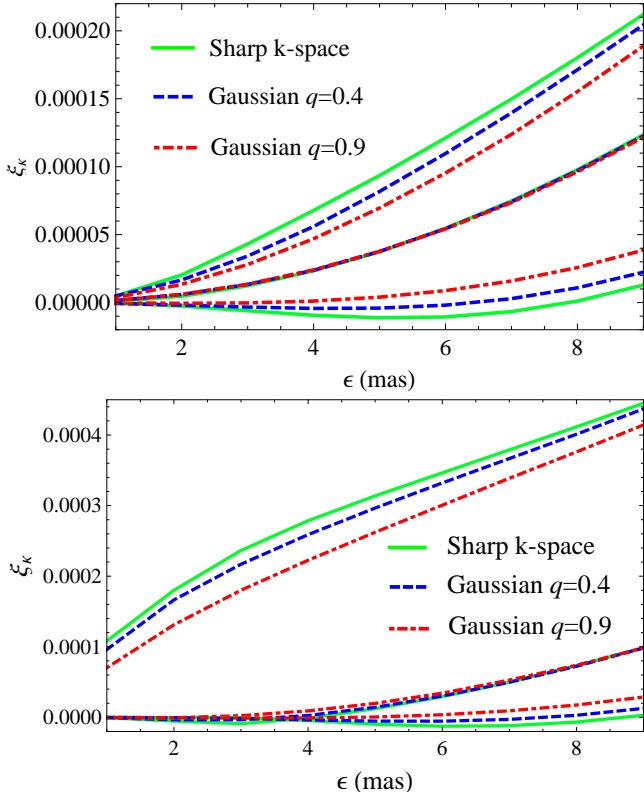


**Figure 11.** 2-point correlation functions of convergence  $\xi_\kappa(\theta)$  for the “Gaussian” filters with  $q = 0.4$  (dashed curves),  $q = 0.9$  (dot-dashed curve) and for the sharp k-space filter (full curve) as a function of the rms shift  $\epsilon$  in the relative position of a pair of images separated by  $\theta$ . The upper and the lower panels show the plots for  $k_{max} = 1000 h\text{Mpc}^{-1}$  and for  $k_{max} = 10000 h\text{Mpc}^{-1}$ , respectively. In each panel, the top, the middle, and the bottom three curves correspond to  $\theta = 0''$ ,  $\theta = 0.5''$ , and  $\theta = 1''$ , respectively. We assume  $z_S = 3$  and  $z_L = 0.5$ .

pair of lensed images with the largest separation angle, as a simple approximation, we adopt a mean separation angle  $\langle\theta\rangle$  between a lensed image and a position of a centroid of the primary lens obtained from all 4 images and their errors in positions as observable quantities that can be used for constraining intervening halos from astrometric shifts<sup>3</sup>. This is because any contribution from fluctuations with angular size similar to the largest separation angle can be taken into account as a part of the constant background convergence and shear. Fluctuations with angular size similar to  $\langle\theta\rangle$  does not contribute to the constant background convergence and shear but they may change the separation angle between a lensed image and the source. In what follows, we also assume that the centroids of MIR images agree with those observed in the visible and near-IR bands.

In this study, we do not use radio QSO lenses, which have been frequently used in literature because the finite source-size effect might be important in analyzing flux-ratios perturbed by intervening clustering halos. The typical size of radio continuum emission region of QSO lenses is  $L \sim 10$  pc. For lens systems with magnifications above  $\mu = 10$ , then the sizes of magnified images can be estimated as  $\gtrsim 3 \times 10$  pc. Assuming that the size of the Einstein radius of is typically  $x_E \sim 5$  kpc, a fractional difference in magnification with respect to a point-source is  $\delta\mu/\mu \sim |\ln(L/x_E)|L/x_E \sim 0.05$  (Inoue & Chiba 2005a) if a top-hat type source with an apparent size  $L = 50$  pc at the lens plane is placed at the center of an SIS. Even in more realistic cases, the order of the difference would be the same as long as the potential has a form similar to an SIS. For instance, the correction term due to differential magnification is proportional to  $L/x_E$  for an SIE lens because we have  $\mu^{-1} \sim 1 - O[x_E/x]$  (Kormann et al. 1994) where  $x$  denotes the radial proper distance from the center of an SIE. Moreover, inclusion of substructure in the primary lens can boost the perturbation by a factor of 2–3 (Metcalf & Amara 2012). Therefore, we expect  $\sim 10$  per cent systematic change in the flux ratios.

The size of continuum emission regions in the MIR band is typically much smaller than radio counterparts. In fact, the estimated source sizes in our sample of MIR lenses are  $L \sim 1$  pc, which is significantly larger than the Einstein radius of stars  $L \sim 0.01$  pc. Therefore, our sample is free from the finite source-size effect and the microlensing effects due to stars. For 5 lenses in our sample, the point-like source approximation is valid at  $\sim 1$  per cent level in flux ratios as long as magnification is not significantly large, i.e.,  $\mu \lesssim 10$ . Moreover, we note that the effect of differential magnification due to intervening halos is negligible as long as the order of shifts in the relative position of images divided by the Einstein radius of the lensing galaxy is  $\delta x/x_E = O(0.001)$  since the magnification perturbation due to shifts of  $\delta x$  can be estimated as  $\delta\mu/\mu \sim \delta x/x_E$ .

As a fiducial model of these lenses, we adopt a singular isothermal ellipsoid (SIE) plus an external shear (ES) (Kormann et al. 1994), which can explain flat rotation

<sup>3</sup> In more realistic setting, we consider light rays that pass through the lensed 4 images (2 saddle and 2 minima) and 1 maximum at the lens plane. Since the position of the maximum is usually close to the centroid of the lensing galaxy, we assume that the corresponding light ray is approximated by a geodesic that pass through the centroid of lensing galaxy.

curves. We use only relative positions of lensed quadruple images and the center of lensing galaxy for modeling. The parameters of the SIE plus ES model are the angular scale of the critical curve or the mass scale inside the critical curve  $b'$ , the ellipticity  $e$  of the lens and its position angle  $\theta_e$ , the strength and the direction of the external shear  $(\gamma, \theta_\gamma)$ , the primary lens position on the lens plane  $(x_0, y_0)$ , and the image position  $(x_i, y_i)$ . The angles  $\theta_e$  and  $\theta_\gamma$  are measured East of North expressed in the observer's coordinates.

It should be emphasized that the observed MIR flux ratios are not used for making best-fit lens models. They are used for only estimating amplitudes of the expected flux anomalies  $\eta$ . To find a set of best-fit parameters, we use a numerical code GRAVLENS<sup>4</sup> developed by Keeton in order to implement the  $\chi^2_{pos}$  fitting of the positions, which have 10 degrees of freedom (8 for quadruple lensed images and 2 for the center of the primary lens). Because the SIE plus ES (SIE-ES) model has 9 degrees of freedom, residual degree of freedom (dof) is 1. If  $\chi^2_{pos}/dof < 2$  cannot be satisfied, we consider either a contribution from a luminous dwarf galaxy X modeled by an SIS with an Einstein radius  $b_X$  in the neighborhood of the primary lens (SIE-ES-X) or introduce a large error for the position of the primary lens in order to satisfy a condition  $\chi^2/dof < 2$  (SIE-ES+). The latter procedure may be verified in some lens systems because any unresolved luminous dwarf galaxies or inhomogeneous structures inside the galactic bulge of lens galaxy would shift the position of the center-of-light from the center of the lens potential.

In what follows, we briefly review our sample of QSO-galaxy lenses and the best-fit models.

### 6.1 B1422+231

This is a cusp caustic lens that produces three colinear bright images A, B, and C with an image opening angle of  $77^\circ.0$  and a faint image D. The source is near a cusp in the astroid-shaped caustic. The observed MIR flux ratios gives  $R_{cusp} = 0.20$  (Chiba et al. 2005). This lens system is the first example that shows a violation of the cusp caustic relation (Mao & Schneider 1998). However, subsequent analysis revealed that the violation is not significant when marginalized over the opening angle and the maximum separation between the three images (Keeton et al. 2003). The redshift of the source  $z_S = 3.62$  (Kundic et al. 1997) is largest in our 6 samples and the primary lens is possibly an elliptical galaxy at  $z_L = 0.34$  (Tonry 1998). Although the positions of images and lens can be well fit by the SIE-ES model (Chiba 2002), the MIR flux ratios between the images A, B, and C are not consistent with the model prediction Chiba et al. (2005). We have confirmed these results and found that inclusion of  $m = 3$  term with the external shear does not improve the fit to the MIR flux ratios. Therefore, it is likely that this lens system is perturbed by matter fluctuations on scales smaller than the separation between the images. Comparing the estimated flux ratios (table 2) to observed ones (table 1), it seems that image A, which is a minimum point in the time arrival surface is most likely to have been magnified by perturbers.

<sup>4</sup> See <http://redfive.rutgers.edu/~keeton/gravlens/>

### 6.2 MG0414+0534

This is a fold caustic lens where a source is placed near an astroid-shaped caustic but not near a cusp in the caustic. The source at a redshift of  $z_S = 2.639$  is lensed by a foreground elliptical galaxy at  $z_L = 0.9584$  (Lawrence et al. 1995; Tonry & Kochanek 1999). It consists of two close bright images A1 and A2 separated by  $0''.415$  and two fainter images B and C. We have found that the SIE-ES model does not give a good fit to the data. In order to improve the fit, we have considered a possible luminous satellite, object X (Schechter & Moore 1993), as has been studied in previous lens models (e.g., Ros et al. (2000)). The object X is modeled by an SIS at  $(x_X, y_X) = (0''.857, 0''.180)$  with an error of  $0''.01$  as taken from CASTLES. The SIE-ES-X model yields a good fit to the positions of images and lens with  $\chi^2 = 0.003$ . However, the MIR flux ratio of A1 to A2 is not consistent with the model prediction. The discrepancy remains even multipoles with  $m = 3$  and  $m = 4$  terms are included (Minezaki et al. 2009). Therefore, it is likely that this lens system is perturbed by matter fluctuations on scales smaller than the separation between images A1 and A2. Comparing the estimated flux ratios (table 2) to observed ones (table 1), it seems that image A2 which is a saddle point in the time arrival surface is most likely to have been demagnified by perturbers.

### 6.3 H1413+117

This is a ‘‘cross’’ lens in which quadruply lensed images have an approximate D4 (dihedral group with 4 rotational symmetries) symmetry. It consists of 4 images, A, B, C, and D. The source redshift is  $z_S = 2.55$  (Magain et al. 1988) but the lens redshift is unknown. We use the data of the MIR flux ratios and the lens position observed by (MacLeod et al. 2009). We have found that the SIE-ES model yields a good fit  $\chi^2/dof = 1.5$  to the data of image and lens positions. However, this model gives a poor fit to the data of the flux ratios. The origin of anomalous flux ratios may be substructures inside the primary lens or clustering halos in the line-of-sight. To circumvent this problem, MacLeod et al. (2009) added an SIS at the position of another galaxy G2 lying at  $(-1''.87, 4''.14)$  with an error of  $0.07''$  from image A, which corresponds to object #14 in Kneib et al. (1998). They have found that  $\chi^2/dof \sim 1$  for image and lens positions, flux ratios, and weak priors for the lens parameters. Goicoechea & Shalyapin (2010), found that time delays between images A-D are also consistent with this model SIE-ES-G2. Assuming a concordance cosmology with the Hubble constant  $H_0 = 70 \text{ km s}^{-1} \text{ Mpc}^{-1}$  and density parameters  $\Omega_m = 0.3$  and  $\Omega_\Lambda = 0.7$ , they estimated the redshift of the primary lens as  $z_l = 1.88^{+0.09}_{-0.11}$ . Although it is not clear whether G2 is the only component that would reproduce the observed flux ratios, we adopt the SIE-ES-G2 model where the position of the center of an SIS is fixed to  $(-1''.87, 4''.14)$  with respect to image A.

### 6.4 PG1115+080

This is a fold caustic lens. The source at a redshift of  $z_S = 1.72$  is lensed by a foreground galaxy at  $z_L = 0.31$  (Kundic et al. 1997). It consists of two close bright images

A1 and A2 separated by  $0''.482$ , and two fainter images B and C. The data of position of images and lens are taken from CASTLES. We find that the SIE-ES model does not provide a good fit to the data unless the error in lens position is increased from  $0.003''$  to  $0.02''$  (SIE-ES+). Interestingly, the value is the same as the  $1\sigma$  error of lens position obtained by (MacLeod et al. 2009) for H1413+117. This may be due to systematic problems in determining the position of the faint lens. As shown by Chiba et al. (2005), the SIE-ES+ model gives a good fit to the positions of the images and the lens and the MIR flux ratios<sup>5</sup>.

### 6.5 Q2237+0305

This is the nearest lens in our sample with a “cross” configuration of four images. The source is located at  $z_S = 1.695$  and the lens at  $z_L = 0.0394$  (Huchra et al. 1985). As shown by Minezaki et al. (2009), the SIE-ES model gives a good fit to the positions of the images and the lens as well as the flux ratios.

### 6.6 RXJ1131-1231

This is a cusp caustic lens with a source at a redshift of  $z_S = 0.658$  lensed by a foreground galaxy at  $z_L = 0.295$  (Sluse et al. 2003). Unfortunately, no data of fluxes due to the MIR continuum emission is available. Instead, we use the data of fluxes of [OIII] emission line from a narrow-line region (NLR) around the source QSO (Sugai et al. 2007). We find that the SIE-ES model does not provide a good fit to the data of positions of images and lens unless the error in the position of the primary lens is increased from  $0.003''$  to  $0.017''$  (SIE-ES+). We find that the SIE-ES+ model gives a good fit to the positions of lensed images but the fit to the flux ratios is turned out to be not sufficiently good. Because the size of the NLR  $\sim 100$  pc is significantly larger than the size of the MIR (near IR in rest frame) continuum emission region ( $\sim 1$  pc), we need a careful consideration on the finite source-size effect. In fact, Sugai et al. (2007) found a possible imprint of an extended structure in the NLR region. The fractional contribution from the extended components can be  $\sim 20\%$  for an aperture of  $0''.77$  for lensed QSO images. The observed “bridge” between image A and image C and a shift of image B in the opposite direction to the critical curve suggest an asymmetric structure of the source. If this effect is taken into account, then the fit to the flux ratios might be improved. This is because the differential magnification of images A and C can lead to a reduction in the flux ratio  $|\mu_A/\mu_C|$  as extended components of the images A and C are nearer to the caustic than the corresponding core components. Thus we expect additional  $\sim 20\%$  uncertainty in the observed flux ratios.

## 7 FLUX-RATIO ANOMALY

In order to measure a possible contribution of clustering halos in the line-of-sight to the flux ratios, we calculate  $\eta$

<sup>5</sup> Alternatively, we may consider a contribution from a nearby group (Sluse et al. 2012).

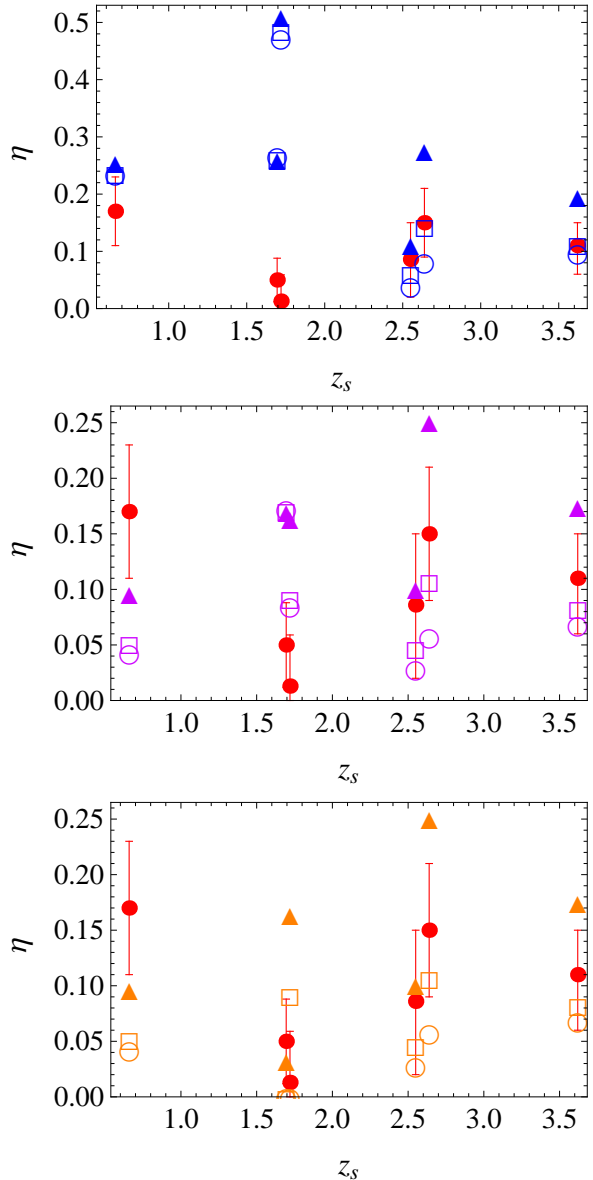


**Figure 12.** Plots of  $\eta$  as a function of a source redshift  $z_S$  for a sample of 6 MIR lenses (disk) and their predicted values for  $k_{max} = 320 h\text{Mpc}^{-1}$  (circle),  $k_{max} = 1000 h\text{Mpc}^{-1}$  (square),  $k_{max} = 10000 h\text{Mpc}^{-1}$  (solid triangle). Top: we assume  $\epsilon = \langle \epsilon \rangle$ , where  $\langle \epsilon \rangle$  is the mean error in relative position of an image and a lens defined for  $N$  images. (table 1). Middle: we assume  $\epsilon = 0.003''$ , a typical value for a lensed image observed in the optical/IR band. Bottom: we assume a cut off  $k_{lens}$  due to lens modeling and  $\epsilon = 0.003''$ . The error bars show the  $1\sigma$  errors in the observed MIR fluxes.

defined in equation (18) for our sample of 6 MIR lenses (5 continuum and 1 line emission). We assume that the errors of the flux ratios and the positions of images and lenses obey the Gaussian statistics. We also assume that non-perturbed lens potentials are given by best-fit models using observed positions of images and lenses. We do not consider any contribution from substructures within a primary lens. Effects of image shifts on the flux ratios due to intervening halos are assumed to be sufficiently small though this assumption

**Table 1.** Observed MIR Flux Ratios

Lens	$z_L$	$z_S$	$N$	Flux Ratio			$\langle \epsilon \rangle$ (")	$\langle \theta \rangle$ (")	Reference
RXJ1131-1231(★)	0.295	0.658	3	A/B $1.63^{+0.04}_{-0.02}$	C/B $1.19^{+0.03}_{-0.12}$		0.017	1.9	1, 2
Q2237+0305	0.04	1.695	4	B/A $0.84 \pm 0.05$	C/A $0.46 \pm 0.02$	D/A $0.87 \pm 0.05$	0.0046	0.9	1, 3
PG1115+080	0.31	1.72	2	A2/A1 $0.93 \pm 0.06$			0.020	1.2	1, 4
H1413+117	1.88(★★)	2.55	4	B/A $0.84 \pm 0.07$	C/A $0.72 \pm 0.07$	D/A $0.40 \pm 0.06$	0.020	0.6	5
MG0414+0534	0.96	2.639	3	A2/A1 $0.90 \pm 0.04$	B/A1 $0.36 \pm 0.02$		0.0042	1.2	1, 3
B1422+231	0.34	3.62	3	A/B $0.94 \pm 0.05$	C/B $0.57 \pm 0.06$		0.0042	1.1	1, 4

References:1. CASTLES; 2. Sugai et al. 2007; 3. Minezaki et al. 2009; 4. Chiba et al. 2005; 5. MacLeod et al. 2009

Note: (★): [OIII] line flux ratios. (★★): The lens redshift  $z_L$  is obtained from a best-fit model using the observed positions of the images and the primary lens, the flux ratios, and the time-delays between the images assuming  $H_0 = 70$  km/s/Mpc.

**Table 2.** Best-fit Model Parameters and Flux Ratios

Model	$b'$ (")	$(x_0, y_0)$ (")	$e$	$\theta_e$ (deg)	$\gamma$	$\theta_\gamma$ (deg)	$b_X$ (")	$dof$ (")	$\chi^2_{pos}$	Flux Ratio		$\langle \mu \rangle$	
RXJ1131-1231 SIE-ES+	1.83	(2.039, 0.568)	0.145	-57.8	0.120	-81.8		1	1.3	A/B 1.66	C/B 0.909	14.6	
Q2237+0305 SIE-ES	0.854	(0.075, 0.939)	0.371	64.9	0.015	-46.8		1	0.004	B/A 0.887	C/A 0.447	D/A 0.825	3.73
PG1115+080 SIE-ES+	1.14	(-0.361, -1.342)	0.156	-83.0	0.110	51.8		1	1.0	A2/A1 0.912		12.5	
H1413+117(★) SIE-ES-X	0.561	(-0.172, -0.561)	0.204	-14.5	0.062	55.7	0.583	2	2.2	B/A 0.894	C/A 0.905	D/A 0.458	5.24
MG0414+0534(★★) SIE-ES-X	1.08	(0.472, -1.277)	0.232	-82.1	0.102	53.8	0.185	0	0.003	A2/A1 1.039	B/A1 0.329	13.1	
B1422+231 SIE-ES	0.755	(-0.741, -0.658)	0.309	-56.6	0.166	-52.3		1	0.55	A/B 0.797	C/B 0.512	4.91	

(★) Object X is modeled by an SIS whose position is fixed at  $(x_X, y_X) = (-1.''87, 4.''14)$ .

(★★) Object X is modeled by an SIS whose position is fitted to  $(x_X, y_X) = (0.''857, 0.''180)$  with an error  $0.''01$ .

might not be valid if the allowed shift is as large as  $\epsilon \sim 0.02''$ . For simplicity, we use the sharp k-space filter for determining the maximum scale of fluctuations that can affect the flux ratios from errors  $\epsilon$  in the relative positions between an image and the center of the primary lens. To obtain the “IR” cutoff  $k_{min}$ , we use a mean separation angle  $\langle \theta \rangle$  of an image and the center of the primary lens and a mean error  $\langle \epsilon \rangle$  in relative positions of an image and the center of the primary lens obtained from quadruple images for each system.

We consider three types of the “UV” cutoff,  $k_{max} = 320, 1000, 10000$   $h\text{Mpc}^{-1}$ .  $k_{max} = 320$   $h\text{Mpc}^{-1}$  corresponds to the Nyquist frequency  $k_{Nyq}$  of our  $N$ -body simulation. For small scale fluctuations with wavenumber  $k > k_{Nyq}$ , we extrapolate the power spectrum obtained in larger scales

$k < k_{Nyq}$ . It should be noted that the extrapolated power spectrum may be systematically larger/smaller than the correct value for  $k > k_{Nyq}$ .  $k_{max} = 10000$   $h\text{Mpc}^{-1}$  corresponds to an Einstein radius  $O[1]$  pc if the corresponding fluctuation forms a point mass. As the source sizes of our MIR samples are  $O[1]$  pc, the contribution of modes  $k > 10000$   $h\text{Mpc}^{-1}$  is expected to be negligible.

As shown in Fig. 12 (top panel), we find that clustering halos with a mass scale of  $M \lesssim O[10^7 M_\odot]$  or  $k > 200$   $h\text{Mpc}^{-1}$  in the line-of-sight are sufficient in explaining the observed anomalies in the flux ratios. However, for Q2237+030 and PG1115+080, the predicted anomalies seem too large unless the rms value of  $\eta$  is at least comparative to the mean. The apparent discrepancy may be due to a

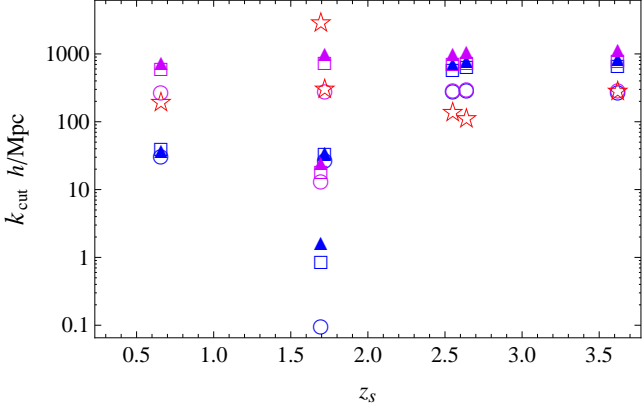


**Figure 13.** Plots of cutoff scales  $k_{cut}$  and the source redshift  $z_S$  for  $\epsilon$  in table (lower, blue) and for  $\epsilon = 0.003''$  (upper, violet) and  $k_{lens}$  (star, red). The “UV cut off” scales are assumed to be  $k_{max} = 320 \text{ hMpc}^{-1}$  (circle),  $k_{max} = 1000 \text{ hMpc}^{-1}$  (square),  $k_{max} = 10000 \text{ hMpc}^{-1}$  (solid triangle).

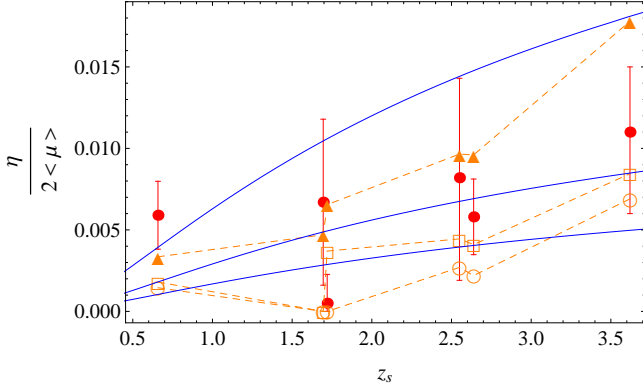


**Figure 14.** Plots of approximated amplitude of convergence  $\sigma_\kappa(0) \sim \eta/2\langle\mu\rangle$  as a function of a source redshift  $z_S$  for the observed MIR lenses (disk) and their predicted values for  $k_{max} = 320 \text{ hMpc}^{-1}$  (circle),  $k_{max} = 1000 \text{ hMpc}^{-1}$  (square),  $k_{max} = 10000 \text{ hMpc}^{-1}$  (solid triangle) assuming  $k_{cut}$  that corresponds to  $\epsilon = 0.003''$  and cut off  $k_{lens}$  due to lens modeling. The error bars show the  $1\sigma$  errors in the observed MIR fluxes. Assuming  $z_L = 0.5$ , rigorous values of  $\sigma_\kappa(0)$  are plotted as full curves for  $(k_{cut}, k_{max}) = (300 \text{ hMpc}^{-1}, 320 \text{ hMpc}^{-1})$  (bottom),  $(750 \text{ hMpc}^{-1}, 1000 \text{ hMpc}^{-1})$  (middle), and  $(1100 \text{ hMpc}^{-1}, 10000 \text{ hMpc}^{-1})$  (top).

possible systematic error in the position of the center of a faint lensing galaxy, which is significantly larger than that of lensed images. A larger error  $\epsilon$  tends to give a larger effect on flux ratios. In order to see this systematic effect, we also calculate  $\eta$  assuming only errors in lensed image positions. In fact, this assumption is reasonable for estimating the abundance of possible line-of-sight halos that reside at the background of lensing galaxy as the faint lensed image of maximum point has not been observed in the 6 lenses. Assuming that  $\epsilon = 0.003''$  for all the 6 lenses (“constant  $\epsilon$ ”), as shown in Fig. 12 (middle panel), we find that the fit to the data of PG1115+080 is greatly improved. However, the fit to the data of Q2237+030 is not improved. This is be-

cause the lens redshift is exceptionally small ( $z_L = 0.04$ ) as compared to other 5 lenses in which  $z_L \approx 0.3 - 2.0$ . As shown in Fig. 13, the cut off scale for Q2237+230 is  $k_{cut} = O[1 - 10] \text{ hMpc}^{-1}$ . This corresponds to mass scales of  $10^{11-13} M_\odot$ , which are similar to mass scales of the primary lens. Therefore, the constraint from the shift of positions is not so stringent. However, we also need to take into account the effect of lens modeling as well. Because a constant convergence and a constant shear of the primary lens are already taken into account in our model, we need to cut off modes that are equal to or larger than the size of the primary lens. For simplicity, we assume that modes with a half wavelength longer than twice the comoving radius of the critical curve  $r(z_L)\theta_E$  of the primary lens are cut off, where  $r(z_L)$  is the comoving distance to the lens at a redshift of  $z_L$ . The corresponding cut off wavenumber is  $k_{lens} \equiv 2\pi/L_{lens}$  where  $L_{lens} \sim 4r(z_L)\theta_E$ .  $\theta_E$  can be estimated as a mean separation angle ( $\theta$ ) between an image and the center of the primary for  $N$  images. As we can see in Fig. 13, the cut off wavenumbers are  $k_{lens} \sim 3100 \text{ hMpc}^{-1}$  for Q2237+030 and  $k_{lens} = O(10^2) \text{ hMpc}^{-1}$  for other 5 systems. This means that the modeling effect is significant for systems in which the lens redshift is exceptionally small. Taking into account the modeling effect in addition to an assumption on the shifts of images and lens  $\epsilon = 0.003''$  positions, we find that the expected  $\eta$  for Q2237+030 is significantly reduced (Fig. 12, bottom panel). Furthermore, the predicted values for the other 5 lenses agree with the data at  $\sim 2\sigma$  level without consideration of run-to-run variance of  $\eta$ . This result does not change even if we use conservative values  $\epsilon = \langle\epsilon\rangle$  as shown in table 1. Moreover, if we cut off the small scale modes  $k > k_{lens}$ , the effect of differential magnification due to shifts of images is negligible in comparison with the flux changes due to the weak lensing since the magnification perturbation due to the shifts of images is given by  $\delta\mu/\mu \sim \delta r/r_E = O(0.001)$ , where the angular size of the lens is  $r_E/r_L \sim 1''$  and the order of the image shift is  $\delta r/r_L \sim O(0.001'')$ .

The result suggests that the flux ratio anomalies are caused by the weak lensing effect due to extragalactic halos with a mass  $M \lesssim 10^7 M_\odot$  in the line-of-sight. In order to see the source redshift  $z_S$  dependence of the flux ratio anomalies, we plot the approximated rms amplitude of convergence due to intervening halos

$$\sigma_\kappa(0) \sim \frac{\eta}{2\langle\mu\rangle}, \quad (37)$$

where  $\langle\mu\rangle$  is the mean magnification obtained from the observed  $N$  images for a best-fit model (see table 2). As shown in Fig. 14, the estimated  $\sigma_\kappa(0)$  from the observed MIR flux ratios monotonically increases as the source redshift  $z_S$  increases and it agrees well with theoretical prediction at  $\sim 2\sigma$  level. It should be noted that the expected amplitude of convergence  $\sigma_\kappa(0)$  for RXJ1131-1231 which shows a deviation at  $\sim 2\sigma$  level might decrease if the finite source-size effect is taken into account as we discussed in section 6 (see also Sugai et al. (2007)).

## 8 CONCLUSIONS AND DISCUSSION

We have studied the weak lensing effect by line-of-sight halos and sub-halos with a mass of  $M \lesssim 10^7 M_\odot$  in QSO-galaxy

strong lens systems with quadruple images in a concordant  $\Lambda$ CDM universe. Using a polynomially fitted non-linear power spectrum  $P(k)$  obtained from  $N$ -body simulations that can resolve halos with a mass of  $M \sim 10^5 M_\odot$ , or structures with a comoving wavenumber  $k = 3.2 \times 10^2 \text{ hMpc}^{-1}$ , we find that the ratio of magnification perturbation due to intervening halos to that of a primary lens is typically  $\eta \sim 0.1$  and the predicted values agree with the estimated values for 6 QSO-galaxy lens systems (continuum emission for 5 lenses, line emission from NLR for 1 lens) with quadruple images in the mid-infrared band without considering the effects of substructures inside the primary lens. The estimated amplitudes of convergence perturbation for the 6 lenses increase with the source redshift as predicted by our semi-analytical model. This feature strongly supports a hypothesis that the observed flux ratio anomalies are caused by intervening halos rather than substructures associated with the primary lens. However, we do not exclude minor effects from substructures especially for systems with low lens redshift  $z_L$  in which the weak lensing effect is small. Using an extrapolated matter power spectrum, we have demonstrated that small halos with a mass of  $M = 10^3 - 10^7 M_\odot$  can significantly affect the magnification ratios of lensed images.

Instead of mass  $M$ , we have used comoving wavenumber  $k$  for parametrizing cut off scale of matter fluctuations due to intervening halos. We have considered two types of cut off,  $k_{cut}$  and  $k_{lens}$ .  $k_{cut}$  is determined from accuracy in positions of lensed images and the primary lens since intervening halos would induce shifts in relative positions of images.  $k_{lens}$  is given by the (effective) Einstein radius of the primary lens. Because large scale fluctuations are taken into account as a constant convergence and a constant shear in lens models, fluctuations that are larger than the Einstein radius should be neglected. Neglecting the shift of the center of a primary lens, we find that  $k_{lens} \lesssim k_{cut} = O[10^2] \text{ hMpc}^{-1}$  for 5 MIR lenses and  $k_{cut} \ll k_{lens} = O[10^3] \text{ hMpc}^{-1}$  for 1 MIR lens in our sample.

We have not used the cusp-caustic relation  $R_{cusp}$  in order to measure the strength of flux ratio anomalies since most of our lens systems have either a complex structure (a luminous satellite) or a broad opening angle  $\theta > 30^\circ$ . Instead, we have devised a new statistic  $\eta$ , to quantify the magnification perturbation. As we need a detailed lens model that fits the observed positions of images and lens, it may sound less generic than using  $R_{cusp}$ . In fact, the mass-sheet degeneracy yields ambiguity in estimating the magnification perturbation. Different models with different radial profiles would certainly give different predictions. However, this is not a problem. As we have discussed, perturbations in convergence and shear  $\delta\kappa, \delta\gamma$  can be measured from extended sources surrounding the MIR continuum emitting region (Inoue & Chiba 2005b). From observed  $\eta$ ,  $\delta\kappa$ , and  $\delta\gamma$ , we would be able to break the mass-sheet degeneracy. This means such an ambiguity can be removed by estimating shifts of lensed images with spatial structures with respect to unperturbed ones.

Because we have used a new statistic  $\eta$  instead of  $R_{cusp}$  it is difficult to directly compare our result with previous studies (Metcalf 2005a; Xu et al. 2012) in which the effect of clustering halos is considered to be minor. However, as our numerically obtained non-linear power spectrum incorporates all the effects of clustering halos and that of their

substructures, our result indicates that clustering effect on mass scales of  $M \lesssim 10^7 M_\odot$  is much important than considered in previous studies. In fact, we observed that our new statistic  $\eta$  is systematically reduced by 20 ~ 30 per cent for  $k_{max} \leq 1000 \text{ hMpc}^{-1}$  and  $z_S > 2.6$  if no correlation between lensed images is not taken into account. Moreover, Xu et al. 2012 considered only the case  $z_S = 2.0$  theoretically though  $z_S$  in our lens systems varies from 0.658 to 3.62. We think that the restriction on the source redshift is one of the weak point in their analysis as the source redshift dependence is the most important factor to probe the contribution from the line-of-sight halos. We have first shown that observed MIR lenses indeed show lens systems with high redshift sources tend to exhibit more anomalous flux ratios than those with low redshift sources. Omitting effects of source redshift dependence, clustering of halos tend to reduce the signal of anomalous flux ratios, on the other hand, neglecting constraints from astrometric shifts or contribution from a constant convergence and shear due to line-of-sight halos (yielding upper limit of mass) tends to increase the signal. Thus, it is difficult to compare our result with the previous works in literature though the conclusion may look similar.

In order to estimate the magnification perturbation constrained from shifts of positions of images and lens, we have considered a ‘‘sharp k-space filter’’ for cutting off the fluctuations on large scales. If we use ‘‘Gaussian filters’’ that are sufficiently smooth, variance in convergence can be systematically decreased than using the ‘‘sharp k-space filter’’. However, if we also consider a cut off due to modeling of a primary lens, such an effect may be negligible as large scale modes are taken into account as a constant convergence or shear. It should be noted that we have neglected effects of 3 point or 4 point correlation of matter fluctuations, which may enhance the flux ratio anomalies. In order to incorporate these effects and check validity of our approximation, we need to implement ray-tracing simulation based on  $N$ -body simulations.

If we include effects of baryons, we naively expect further enhancement in magnification perturbation as baryon cooling would steepen the gravitational potential of halos at small scales (Rudd et al. 2008; Semboloni et al. 2011; van Daalen et al. 2011). Then our result would give a lower limit of the amplitude of perturbation in magnification ratios. However, feedback from supernovae or super massive black holes could suppress such a steepening near the center of halo due to outflows (Booth & Schaye 2009). This might eventually suppress the magnification perturbation due to line-of-sight halos. Thus in order to improve our  $N$ -body simulations using only collisionless dark matter particles, it is very important to incorporate baryonic physics down to mass scale of  $\sim 10^3 M_\odot$  or less. In other words, small scale baryonic physics which is relevant to galaxy formation might be gravitationally probed by the weak lensing effect in QSO-galaxy strong lensing system in the near IR or MIR band.

Next generation telescopes such as the European Extreme Large Telescope (E-ELT) (Gilmozzi & Spyromilio 2007) or Thirty Meter Telescope (TMT) (Crampton & Ellerbroek 2006) can be used to probe hundreds of such strong lens systems that are too faint for currently available largest telescopes to observe.

They will provide us a unique probe into clustering property of mini-halos with a mass of  $M < 10^6 M_\odot$ .

## 9 ACKNOWLEDGMENTS

We acknowledge useful comments from Masashi Chiba, Takeo Minezaki, and Joseph Silk. We also thank Takahiro Nishimichi for kindly providing us the 2LPT code and an anonymous referee for finding various typos in the manuscript. This work was supported in part by Hirosaki University Grant for Exploratory Research by Young Scientists, by the Grant-in-Aid for Scientific Research on Priority Areas No. 467 “Probing the Dark Energy through an Extremely Wide and Deep Survey with Subaru Telescope”, by the Grand-in-Aid for the Global COE Program “Quest for Fundamental Principles in the Universe: from Particles to the Solar System and the Cosmos” from the Ministry of Education, Culture, Sports, Science and Technology (MEXT) of Japan, by the MEXT Grant-in-Aid for Scientific Research on Innovative Areas (No. 21111006), by the FIRST program “Subaru Measurements of Images and Redshifts (SuMIRe)”. Numerical computations were carried out on SR16000 at YITP in Kyoto University and Cray XT4 at Center for Computational Astrophysics, CfCA, of National Astronomical Observatory of Japan.

## APPENDIX A: FUNCTIONAL FORM OF FITTING FUNCTION

In this Appendix, we provide the functional form of our fitting function of the non-linear matter power spectrum  $P(k)$ . The fitting function can be used up to a wavenumber of  $k = 320 h\text{Mpc}^{-1}$ , at  $0 \leq z \leq 4$  for a concordant cosmological model with  $(\Omega_m, \Omega_b, \Omega_\Lambda, h, n_s, \sigma_8) = (0.272, 0.046, 0.728, 0.70, 0.97, 0.81)$ , which are obtained from the observed WMAP 7yr result (Jarosik et al. 2011), the baryon acoustic oscillations (Percival et al. 2010), and  $H_0$  (Riess et al. 2009).

The non-linear power spectrum has been frequently calculated using the halo-fit model by Smith et al. (2003) (hereinafter, S03), which has 30 fitting parameters to fit the power spectrum obtained from their  $N$ -body simulations. However, as already pointed out by many authors (see, Introduction in Takahashi et al. 2012), the halo-fit model underestimates the power spectrum in comparison with the values from the latest simulations at small scales  $k \gtrsim 0.1 h\text{Mpc}^{-1}$ . This is because the resolution of simulation in S03 is lower than that of the recent simulations. Recently, Takahashi et al. (2012) have provided an improved halo-fit model based on the original halo-fit model but re-calculated the fitting parameters to match their latest simulation results. However, their model can be used for only wavenumbers of  $k < 30 h\text{Mpc}^{-1}$ , which is not sufficient for our purpose. Our interest is in the galactic scale, which corresponds to  $k > 100 h\text{Mpc}^{-1}$ . In this Appendix, we provide a fitting function that can be used to calculate the power spectrum at wavenumbers  $k \leq 320 h\text{Mpc}^{-1}$ . Our fitting function is based on the original halo-fit model (S03), but slightly change the parameters in their model to fit our simulation results.

In the halo-fit model (S03), the dimensionless non-linear

power spectrum,  $\Delta^2(k) = k^3 P(k)/(2\pi^2)$  consists of one- and two-halo terms:

$$\Delta^2(k) = \Delta_Q^2(k) + \Delta_H^2(k). \quad (\text{A1})$$

The first term is the two-halo term which dominates on large scales, while the second term is the one-halo term which dominates on small scales. We changed the one-halo term to fit our simulation results on small scales. In S03, there are four parameters  $a_n, b_n, c_n, \gamma_n$  in the one-halo term. These four parameters are given by as polynomial functions of an effective spectrum index  $n_{\text{eff}}$  and curvature  $C$  calculated by the input linear power spectrum (see Appendix of S03 for details). There are 17 coefficients in the polynomials, and we will determine these 17 parameters to fit our simulation results.

In order to obtain the fitting function, we use four simulation results: three simulations with  $L = 10 h\text{Mpc}^{-1}$  presented in this paper (see section 4), and another from the work of Takahashi et al. (2012). For the four simulations, we adopt the same cosmological model as we have mentioned. The present three simulations with  $L = 10 h\text{Mpc}^{-1}$  are used for fitting on small scales  $k > 30 h\text{Mpc}^{-1}$  while the other one is used on large scales  $k < 30 h\text{Mpc}^{-1}$ . The fitting parameters are obtained by using the standard chi-squared analysis. The chi-square is defined as

$$\chi^2 = \sum_i \sum_{k,z} \frac{[P_{\text{model}}(k, z) - P_{i,\text{sim}}(k, z)]^2}{2\sigma_i^2(k, z)}, \quad (\text{A2})$$

where  $P_{\text{model}}$  is the model prediction, and  $P_{i,\text{sim}}$  is the four simulation results labeled with an integer  $i = 1 - 4$ . We sum up the powers at eight redshifts  $z = 0, 0.35, 0.7, 1, 1.5, 2.2, 3, 4^6$  and simply set the variance  $\sigma_i^2 = P_{i,\text{sim}}^2$  to give an equal weight for all the scales.

For the three simulations with  $L = 10 h\text{Mpc}^{-1}$ , we sum up  $k$  to the Nyquist frequency  $k_{\text{Nyq}} = 320(160) h\text{Mpc}^{-1}$  for  $N_p^3 = 1024^3(512^3)$ . On large scales  $k \lesssim 10 h\text{Mpc}^{-1}$ , the sample variance among the three simulations is very large (over some tens percent) since our simulation box is very small ( $10 h^{-1}\text{Mpc}$  on a side). Hence, we use the simulation results in the wavenumber where the sample variance is smaller than 16%, which corresponds to  $k > 50 h\text{Mpc}^{-1}$  for all the redshifts.

We also use the simulation results from Takahashi et al. (2012) on large scales  $k < 30 h\text{Mpc}^{-1}$ . Using the same simulation codes as ours, they employed  $1024^3$  particles in simulation boxes  $L = 2000, 800, 320 h^{-1}\text{Mpc}$  on a side and combined the  $P(k)$  from the different box sizes to cover a wide range of scales. They prepared 6(3) realizations for  $L = 320(800, 2000) h^{-1}\text{Mpc}$  and gave the mean power spectrum among the realizations up to  $k = 30 h\text{Mpc}^{-1}$ . In order to reduce the shot noise effect, they did not use the simulation results at high wavenumbers  $k$ : the upper limits of the wavenumber are  $k_{\text{max}} = 30 h\text{Mpc}^{-1}$  at  $z = 0, 0.35$ ,  $k_{\text{max}} = 20 h\text{Mpc}^{-1}$  at  $z = 0.7, 1$ ,  $k_{\text{max}} = 10 h\text{Mpc}^{-1}$  at  $z = 1.5, 2.2$  and  $k_{\text{max}} = 8 h\text{Mpc}^{-1}$  at  $z = 3$  in which the power spectrum is 10 times larger than the shot noise.

Using the standard chi-squared analysis in Eq.(A2), we

<sup>6</sup> We do not use an output at  $z = 0$  for one simulation of  $N_p^3 = 1024^3$  in  $L = 10 h^{-1}\text{Mpc}$  because of limit in CPU time.



find the best-fit parameters:

$$\begin{aligned}
 \log_{10} a_n &= 2.576 + 2.263n_{\text{eff}} + 1.452n_{\text{eff}}^2 + 0.6308n_{\text{eff}}^3 \\
 &\quad + 0.1542n_{\text{eff}}^4 - 1.912C, \\
 \log_{10} b_n &= 2.062 + 1.034n_{\text{eff}} + 0.2651n_{\text{eff}}^2 - 3.677C, \\
 \log_{10} c_n &= 0.4449 + 1.743n_{\text{eff}} + 0.6772n_{\text{eff}}^2 + 0.06859C, \\
 \gamma_n &= 0.2174 - 0.1366n_{\text{eff}} + 0.2418C. \quad (\text{A3})
 \end{aligned}$$

The other parameters such as  $\alpha_n, \beta_n, \mu_n, \nu_n, f(\Omega)$  are the same as in S03. The definitions of the effective spectrum index  $n_{\text{eff}}$  and curvature  $C$  are given in the Appendix of S03.

One can see in Fig.2 that our fitting formula agrees well with our simulation results. In fact, the root-mean-square deviation of our best-fit model of  $\Delta^2(k)$  from our simulation results is just 5.1% and the maximum deviation is 20% at  $k \sim 50 \text{ hMpc}^{-1}$  due to the lack of available number of modes comparable to the simulation box size.

## REFERENCES

- Amara A., Metcalf R. B., Cox T. J., Ostriker J. P., 2006, Monthly Notices of the Royal Astronomical Society, 367, 1367
- Bartelmann M., Schneider P., 2001, Physics Reports, 340, 291
- Booth C. M., Schaye J., 2009, Monthly Notices of Royal Astronomical Society, 398, 53
- Bullock J. S., Kravtsov A. V., Weinberg D. H., 2000, Astrophysical Journal, 539, 517
- Busha M. T., Alvarez M. A., Wechsler R. H., Abel T., Strigari L. E., 2010, Astrophysical Journal, 710, 408
- Chen J., 2009, Astronomy & Astrophysics, 498, 49
- Chen J., Koushiappas S. M., Zentner A. R., 2011, Astrophysical Journal, 741, 117
- Chen J., Kravtsov A. V., Keeton C. R., 2003, Astrophysical Journal, 592, 24
- Chiba M., 2002, The Astrophysical Journal, 565, 17
- Chiba M., Minezaki T., Kashikawa N., Kataza H., Inoue K. T., 2005, Astrophysical Journal, 627, 53
- Crampton D., Ellerbroek B., 2006, in Whitelock P., Dennefeld M., Leibundgut B., eds, IAU Symposium NO.232, 2005 Vol. 232, Design and development of tmtf. Cambridge University Press, p. 410
- Crocce M., Pueblas S., Scoccimarro R., 2006, Monthly Notices of the Royal Astronomical Society, 373, 369
- D’Onghia E., Springel V., Hernquist L., Keres D., 2010, Astrophysical Journal, 709, 1138
- Eisenstein D. J., Hu W., 1999, Astrophysical Journal, 511, 5
- Gilmozzi R., Spyromilio J., , 2007, The 42 m European ELT: status
- Goicoechea L. J., Shalyapin V. N., 2010, Astrophysical Journal, 708, 995
- Hisano J., Inoue K. T., Takahashi T., 2006, Physics Letters B, 643, 141
- Huchra J., Gorenstein M., Kent S., Shapiro I., Smith G., Horine E., Perley R., 1985, Astronomical Journal, 90, 691
- Inoue K. T., Chiba M., 2005a, Astrophysical Journal, 633, 23
- Inoue K. T., Chiba M., 2005b, Astrophysical Journal, 634, 77
- Jarosik N., Bennett C. L., Dunkley J., Gold B., Greason M. R., Halpern M., Hill R. S., Hinshaw G., Kogut A., Komatsu E., Larson D., Limon M., Meyer S. S., Nolte M. R., Odegard N., Page L., Smith K. M., Spergel D. N., Tucker G. S., Weiland J. L., Wollack E., Wright E. L., 2011, Astrophysical Journal Supplement Series, 192, 1
- Keeton C. R., Gaudi B. S., Petters A. O., 2003, Astrophysical Journal, 598, 138
- Kneib J. P., Alloin D., Mellier Y., Guilloteau S., Barvainis R., Antonucci R., 1998, Astronomy and Astrophysics, 329, 827
- Kormann R., Schneider P., Bartelmann M., 1994, Astronomy and Astrophysics, 284, 285
- Kundic T., Cohen J. G., Blandford R. D., Lubin L. M., 1997, Astronomical Journal, 114, 507
- Kundic T., Hogg D. W., Blandford R. D., Cohen J. G., Lubin L. M., Larkin J. E., 1997, Astronomical Journal, 114, 2276
- Lawrence C. R., Elston R., Januzzi B. T., Turner E. L., 1995, Astronomical Journal, 110, 2570
- Maccio A. V., Miranda M., 2006, Monthly Notices of the Royal Astronomical Society, 368, 599
- McKean J. P., Koopmans L. V. E., Flack C. E., Fassnacht C. D., Thompson D., Matthews K., Blandford R. D., Readhead A. C. S., Soifer B. T., 2007, Monthly Notices of the Royal Astronomical Society, 378, 109
- MacLeod C. L., Kochanek C. S., Agol E., 2009, Astrophysical Journal, 703, 1177
- Magain P., Surdej J., Swings J. P., Borgeest U., Kayser R., Kuhr H., Refsdal S., Remy M., 1988, Nature, 334, 325
- Mao S., Schneider P., 1998, Monthly Notices of the Royal Astronomical Society, 295, 587
- Metcalf R. B., 2005a, The Astrophysical Journal, 629, 673
- Metcalf R. B., 2005b, The Astrophysical Journal, 622, 72
- Metcalf R. B., Amara A., 2012, Monthly Notices of the Royal Astronomical Society, 419, 3414
- Metcalf R. B., Madau P., 2001, The Astrophysical Journal, 563, 9
- Metcalf R. B., Moustakas L. A., Bunker A. J., Parry I. R., 2004, Astrophysical Journal, 607, 43
- Minezaki T., Chiba M., Kashikawa N., Inoue K. T., Kataza H., 2009, Astrophysical Journal, 697, 610
- Miranda M., Maccio A. V., 2007, Monthly Notices of the Royal Astronomical Society, 382, 1225
- More A., McKean J. P., More S., Porcas R. W., Koopmans L. V. E., Garrett M. A., 2009, Monthly Notices of the Royal Astronomical Society, 394, 174
- Navarro J. F., Frenk C. S., White S. D. M., 1997, Astrophysical Journal, 490, 493
- Nishimichi T., Shirata A., Taruya A., Yahata K., Saito S., Suto Y., Takahashi R., Yoshida N., Matsubara T., Sugiyama N., Kayo I., Jing Y. P., Yoshikawa K., 2009, Publications of the Astronomical Society of Japan, 61, 321
- Press W. H., Schechter P., 1974, Astrophysical Journal, 187, 425
- Riess A. G., Macri L., Casertano S., Sosey M., Lampeitl H., Ferguson H. C., Filippenko A. V., Jha S. W., Li W. D., Chornock R., Sarkar D., 2009, Astrophysical Journal, 699, 539

- Ros E., Guirado J. C., Marcaide J. M., Perez-Torres M. A., Falco E. E., Munoz J. A., Alberdi A., Lara L., 2000, *Astronomy and Astrophysics*, 362, 845
- Rudd D. H., Zentner A. R., Kravtsov A. V., 2008, *Astronomical Journal*, 672, 19
- Schechter P. L., Moore C. B., 1993, *Astronomical Journal*, 105, 1
- Semoloni E., Hoekstra H., Schaye J., van Daalen M. P., McCarthy I. G., 2011, *Monthly Notices of Royal Astronomical Society*, 417, 2020
- Sheth R. K., Tormen G., 2002, *Monthly Notices of the Royal Astronomical Society*, 329, 61
- Shin E. M., Evans N. W., 2008, *Monthly Notices of the Royal Astronomical Society*, 390, 505
- Sluse D., Chantry V., Magain P., Courbin F., Meylan G., 2012, *Astronomy and Astrophysics*, 538, A99
- Sluse D., Surdej J., Claeskens J. F., Hutsemekers D., Jean C., Courbin F., Nakos T., Billeres M., Khmil S. V., 2003, *Astronomy and Astrophysics*, 406, L43
- Smith R. E., Peacock J. A., Jenkins A., White S. D. M., Frenk C. S., Pearce F. R., Thomas P. A., Efstathiou G., Couchman H. M. P., 2003, *Monthly Notices of the Royal Astronomical Society*, 341, 1311
- Springel V., 2005, *Monthly Notices of the Royal Astronomical Society*, 364, 1105
- Springel V., Yoshida N., White S. D. M., 2001, *New Astronomy*, 6, 79
- Sugai H., Kawai A., Shimono A., Hattori T., Kosugi G., Kashikawa N., Inoue K. T., Chiba M., 2007, *Astrophysical Journal*, 660, 1016
- Takahashi R., Sato M., Nishimichi T., Taruya A., Oguri M., *Astrophysical Journal*, submitted (arXiv:1208.2701), 2012
- Tonry J. L., 1998, *Astronomical Journal*, 115, 1
- Tonry J. L., Kochanek C. S., 1999, *Astronomical Journal*, 117, 2034
- Valageas P., Nishimichi T., 2011, *Astronomy and Astrophysics*, 527, 87
- van Daalen M. P., Schaye J., Booth C. M., Dalla Vecchia C., 2011, *Monthly Notices of Royal Astronomical Society*, 415, 3649
- Vegetti S., Lagattuta D. J., McKean J. P., Auger M. W., Fassnacht C. D., Koopmans L. V. E., 2012, *Nature*, 481, 341
- Wong K. C., Keeton C. R., Williams K. A., Momcheva I. G., Zabludoff A. I., 2011, *Astrophysical Journal*, 726, 84
- Xu D., Mao S., Wang J., Springel V., Gao L., White S., Frenk C., Jenkins A., Li G., Navarro J., 2009, *Monthly Notices of the Royal Astronomical Society*, 398, 1235
- Xu D. D., Mao S., Cooper A. P., Gao L., Frenk C. S., Angulo R. E., Helly J., 2012, *Monthly Notices of the Royal Astronomical Society*, 421, 2553
- Xu D. D., Mao S. D., Cooper A. P., Wang J., Gao L. A., Frenk C. S., Springel V., 2010, *Monthly Notices of the Royal Astronomical Society*, 408, 1721